ELSEVIER

Comput. Methods Appl. Mech. Engrg. 138 (1996) 273–298

Computer methods in applied mechanics and engineering

Hierarchical modeling of heterogeneous bodies

Tarek I. Zohdi*,[1], J. Tinsley Oden[2], Gregory J. Rodin[3]

Texas Institute for Computational and Applied Mathematics, The University of Texas at Austin, Austin, TX 78712, USA

Received 15 May 1996

Abstract

In this paper, a methodology is introduced for the development of adaptive methods for hierarchical modeling of elastic heterogeneous bodies. The approach is based on the idea of computing an estimate of the modeling error introduced by replacing the actual fine-scale material tensor with that of a homogenized material, and to adaptively refine the material description until a prespecified error tolerance is met. This process generates a family of coarse-scale solutions in which the solution corresponding to the fine-scale model of the body, which embodies the exact microstructure, loading and boundary conditions, represents the highest level of sophistication in a family of continuum models. The adaptive strategy developed can lead to a new non-uniform description of material properties which reflects the loading and boundary conditions. A post-processing technique is also introduced which endows the coarse-scale solutions with fine-scale information, through a local solution process. Convergence of the adaptive algorithm is proven and modeling error estimates as a function of scale of material description are presented. Preliminary results of several numerical experiments are given to confirm estimates and to illustrate the promise of the approach in practical applications.

1. Introduction

In structural materials, the presence of fine-scale features, whether introduced by design or occurring naturally, can greatly affect properties of the material, such as stiffness, yield strength, ultimate strength and fracture toughness. In particulate and fiber-reinforced composites, macroscopic features of failure are commonly thought to be linked to microscopic damage features which preferentially nucleate at particle/matrix and fiber/matrix interfaces. Unfortunately, if all of the detailed microscale interactions are taken into account in an analysis of the response of a structure, a problem of enormous size and complexity is typically encountered which far exceeds the capacity of the largest supercomputers available or expected to be available for many generations.

Because of this fact the use of *homogenized* material properties are commonplace in classical engineering analysis and design. Methods of homogenization are, of course, the foundation of the theory of composite materials and they have been the object of much study and discussion for many years. An account of the essentials of the theory, and its variants, can be found in [8]. Although homogenization techniques have been proven effective in the determination of overall properties, it is obvious that fine-scale features are completely missed when using homogenized material properties in stress analyses. Consequently, it is unreasonable to expect that the use of uniform material properties can accurately capture local behavior necessary for realistic estimates of a structure's useful life. For very sensitive applications, numerical simulation, incorporating fine-scale features have been used to

* Corresponding author. E-mail: tarek@ticam.utexas.edu

[1] Research Assistant and CAM Fellow.

[2] Director of TICAM, Cockrell Family Regents Chair # 2 in Engineering.

[3] Associate Professor, Aerospace Engineering and Engineering Mechanics.

PII S0045-7825(96)01106-1

resolve stress and strain fields throughout a body. There have been early attempts to incorporate fine-scale features in a global analysis. Noteworthy are the representative works of Fish and Belsky [1,2], based on multigrid methods, and Ghosh and Moorthy [3,4] whose techniques are based on Voronoi-cell finite elements.

In the present work, a method for obtaining solutions to problems in elastostatics involving bodies composed of heterogeneous materials is developed. The approach is based on the idea of computing an estimate of the *modeling error* introduced by replacing the actual fine-scale material tensor with that of a homogenized material, and, to successively refine the material properties until a preset error tolerance has been met. The method is a technique of hierarchical modeling, in which the fine-scale model of a structural component, which embodies the exact microstructure, loading and boundary conditions represents the highest level of sophistication in a family of methods.

Specifically, the approach consists of three steps, which are presented in the following order:

(1) We first derive an explicit expression for an upper bound on the difference in a solution generated by solving a linear elastostatics problem with a homogeneous elasticity tensor (the coarse-scale solution) and solution generated by solving the same boundary value problem with the actual elasticity tensor (the fine-scale solution). It is shown that this modeling error estimate provides a global upper bound. Also, preliminary numerical experiments suggest that the estimate gives an adequate resolution of the local error. This bound is shown to hold, independently of the loading and boundary conditions, for any choice of an approximate elasticity tensor (not necessarily constant), provided that it satisfies standard ellipticity conditions.

(2) A technique is then developed to generate intermediate scales of the material description, a hierarchical family, which produces a sequence of boundary value problems whose solutions convergence to the fine-scale solution, in an energy norm. Scale-dependent modeling error estimates are presented.

(3) Finally, a relatively inexpensive post-processing technique is developed, which is designed to take advantage of the wide availability of parallel processing platforms. The method supplies the coarse-scale solutions produced by the hierarchical process with fine-scale information through a local solution process, where the *exact* material properties are used. This process can be thought of as either a local perturbation method, or, as a non-overlapping domain decomposition technique [9].

The results of several preliminary numerical experiments are given to confirm estimates and to illustrate the possible effectiveness of the presented approaches in practical applications. A fundamental point of the presented work is that the error in solutions produced by classical homogenization methods can be estimated and that the quality of the response can be improved by systematically accounting for effects of fine-scale features of the material.

2. Preliminaries

2.1. Notations and conventions

Throughout this work we use the $L^2(\Omega)$-based Sobolev spaces $H^m(\Omega)$ consisting of functions with generalized partial derivatives of order less than or equal to m in $L^2(\Omega)$ defined on an open domain $\Omega \in \mathbb{R}^N$; $N = 1$, 2 or 3. These spaces are equipped with the usual norms and seminorms

$$\|u\|^2_{H^m(\Omega)} = \int_\Omega \sum_{|\alpha| \le m} |D^\alpha u|^2 \, d\boldsymbol{x} \quad \text{and} \quad |u|^2_{H^m(\Omega)} = \int_\Omega \sum_{|\alpha| = m} |D^\alpha u|^2 \, d\boldsymbol{x} . \tag{1}$$

We also use the spaces $H^s(\Omega)$ for non-integer $s \in \mathbb{R}$.

As is standard, $C_0^m(\Omega)$ is the subspace of $C^m(\Omega)$ consisting of functions with compact support in Ω. The closure of $C_0^m(\Omega)$ with respect to the $H^m(\Omega)$ norm in $H^m(\Omega)$ is denoted $H_0^m(\Omega)$ and the duals of the spaces $H_0^m(\Omega)$ are the negative Sobolev spaces $H^{-m}(\Omega)$. All spaces appearing in boldface are

vector-valued extensions of the preceding ideas. For example, $\boldsymbol{H}^m(\Omega) = [H^m(\Omega)]^N$ is the space of vector-valued functions whose components have partial derivatives of order less than or equal to m in $\boldsymbol{L}^2(\Omega) = [L^2(\Omega)]^N$. Accordingly,

$$\|\boldsymbol{v}\|^2_{H^m(\Omega)} = \sum_{i=1}^{N} \|v_i\|^2_{H^m(\Omega)} \quad \text{and} \quad |\boldsymbol{v}|^2_{H^m(\Omega)} = \sum_{i=1}^{N} |v_i|^2_{H^m(\Omega)} . \tag{2}$$

For the inner product of tensors $\nabla \boldsymbol{u}, \nabla \boldsymbol{v} \in [L^2(\Omega)]^{N\times N}$, $\boldsymbol{u}, \boldsymbol{v} \in \boldsymbol{H}^1(\Omega)$, we use the following notation,

$$\nabla \boldsymbol{v} : \nabla \boldsymbol{u} = \mathbf{tr}[(\nabla \boldsymbol{v})^{\mathrm{T}} \nabla \boldsymbol{u}] = \sum_{i,j=1}^{N} \frac{\partial u_i}{\partial x_j} \frac{\partial v_i}{\partial x_j} \in L^1(\Omega) , \tag{3}$$

where $\partial u_i/\partial x_j$, $\partial v_i/\partial x_j$ are generalized partial derivatives of u_i and v_i, $1 \leqslant i, j \leqslant N$, and where u_i, v_i are Cartesian components of $\boldsymbol{u}$ and $\boldsymbol{v}$. Throughout this paper we shall use the symbol '$\boldsymbol{v}|_{\partial\Omega}$' for boundary values of $\boldsymbol{v} \in \boldsymbol{H}^m(\Omega)$, where boundary values are interpreted in the sense of traces.

2.2. Linear elasticity

We consider a material body composed of a linearly-elastic material and in static equilibrium under the action of body forces $\boldsymbol{f}$ and surface tractions $\boldsymbol{t}$. The body occupies an open bounded domain in $\Omega \in \mathbb{R}^N$ and its boundary is denoted $\partial\Omega$. For present purposes, it suffices to consider cases of which Ω is regular: a simply-connected domain with Lipschitz boundary. The boundary $\partial\Omega$ consists of a portion Γ_u where the displacements are prescribed and a part Γ_t where tractions are prescribed,

$$\partial\Omega = \overline{\Gamma_u \cup \Gamma_t} \qquad \Gamma_u \cup \Gamma_t = \emptyset . \tag{4}$$

The data are assumed to be such that $\boldsymbol{f} \in \boldsymbol{L}^2(\Omega)$, $\boldsymbol{t} \in \boldsymbol{L}^2(\Gamma_t)$.

The space of admissible displacements, $\boldsymbol{V}(\Omega)$, consists of those displacement fields in the space $\boldsymbol{H}^1(\Omega)$ which satisfy homogeneous (displacement) boundary conditions on Γ_u,

$$\boldsymbol{V}(\Omega) = \{\boldsymbol{v} \in \boldsymbol{H}^1(\Omega) : \boldsymbol{v}|_{\Gamma_u} = 0\} . \tag{5}$$

The displacements on Γ_u are prescribed as follows: $\exists \hat{\boldsymbol{u}} \in \boldsymbol{H}^1(\Omega)$,

$$\boldsymbol{u}|_{\Gamma_u} = \hat{\boldsymbol{u}}|_{\Gamma_u} = \mathcal{U} , \tag{6}$$

where $\mathcal{U}$ is specified displacement data on Γ_u. Thus, the actual displacements of the body are in the translation $\{\hat{\boldsymbol{u}}\} + \boldsymbol{V}(\Omega)$.

We consider the classical principle of virtual work characterized by the following variational boundary-value problem of elastostatics:

$$\boxed{\begin{array}{l} \text{Find } \boldsymbol{u} \in \{\hat{\boldsymbol{u}}\} + \boldsymbol{V}(\Omega) \text{ such that} \\ \mathcal{B}(\boldsymbol{u}, \boldsymbol{v}) = \mathcal{F}(\boldsymbol{v}) \quad \forall\, \boldsymbol{v} \in \boldsymbol{V}(\Omega) . \end{array}} \tag{7}$$

Here, $\mathcal{B} : \boldsymbol{H}^1(\Omega) \times \boldsymbol{H}^1(\Omega) \mapsto \mathbb{R}$ is the bilinear form characterizing the virtual work and $\mathcal{F}(\cdot)$ is a linear functional characterizing the work done by the external forces,

$$\mathcal{B}(\boldsymbol{u}, \boldsymbol{v}) = \int_\Omega \nabla \boldsymbol{v} : \boldsymbol{E} \nabla \boldsymbol{u} \, \mathrm{d}\boldsymbol{x} \qquad \mathcal{F}(\boldsymbol{v}) = \int_\Omega \boldsymbol{f} \cdot \boldsymbol{v} \, \mathrm{d}\boldsymbol{x} + \int_{\Gamma_t} \boldsymbol{t} \cdot \boldsymbol{v} \, \mathrm{d}s , \tag{8}$$

where the mechanical (stress–strain) properties of the material are characterized by the elasticity tensor $\boldsymbol{E}$ which is assumed to be a given function in $[L^\infty(\Omega)]^{N^2\times N^2}$.

If the data in (7) are smooth and if (7) possesses a solution $\boldsymbol{u}$ that is sufficiently regular, then $\boldsymbol{u}$ is the solution of the classical linear elastostatics problem,

$$\boxed{\begin{aligned} &-\nabla\cdot(\boldsymbol{E}(\boldsymbol{x})\nabla\boldsymbol{u}(\boldsymbol{x})) = \boldsymbol{f}(\boldsymbol{x}) \quad \boldsymbol{x}\in\Omega \\ &\boldsymbol{u}(\boldsymbol{x}) = \mathcal{U}(\boldsymbol{x}) \quad \boldsymbol{x}\in\Gamma_u \\ &\boldsymbol{n}\cdot(\boldsymbol{E}\nabla\boldsymbol{u}(\boldsymbol{x})) = \boldsymbol{t}(\boldsymbol{x}) \quad \boldsymbol{x}\in\Gamma_t\,. \end{aligned}} \tag{9}$$

2.2.1. The elasticity tensor

The elasticity tensor in (8) characterizes the mechanical properties of the material and, for materials with highly heterogeneous microstructures, can be highly oscillatory. We require that the elasticities be subject to the following ellipticity and symmetry conditions: $\exists\alpha_\ell$, $\alpha_v>0$ such that $\forall\boldsymbol{A}\in\mathbb{R}^{N\times N}$, $\boldsymbol{A}=\boldsymbol{A}^{\mathrm{T}}$ (a.e. $\boldsymbol{x}\in\bar{\Omega}$),

$$\boxed{\begin{aligned} &\alpha_v\boldsymbol{A}:\boldsymbol{A}\geqslant\boldsymbol{A}:\boldsymbol{E}(\boldsymbol{x})\boldsymbol{A}\geqslant\alpha_\ell\boldsymbol{A}:\boldsymbol{A}\,, \\ &E_{ijkl}(\boldsymbol{x}) = E_{jikl}(\boldsymbol{x}) = E_{ijlk}(\boldsymbol{x}) = E_{klij}(\boldsymbol{x}) \quad 1\leqslant i,j,k,l\leqslant N\,, \end{aligned}} \tag{10}$$

$E_{ijkl}(\boldsymbol{x})$ being the Cartesian components of $\boldsymbol{E}$ at point $\boldsymbol{x}$.

2.2.2. Homogenization

The problem described by (7) is usually far too complex to be solved by conventional computational methods due to the complex internal geometry of the body, characterized by a highly variable $\boldsymbol{E}$. To perform an analysis of the response of the structure it is customary to replace $\boldsymbol{E}$ by a uniform 'effective' elasticity tensor, denotes $\boldsymbol{E}^0$. This leads to a new more tractable problem,

$$\boxed{\begin{aligned} &\text{Find } \boldsymbol{u}^0\in\{\hat{\boldsymbol{u}}\}+\boldsymbol{V}(\Omega) \text{ such that} \\ &\mathcal{B}^0(\boldsymbol{u}^0,\boldsymbol{v}) = \mathcal{F}(\boldsymbol{v}) \quad \forall\,\boldsymbol{v}\in\boldsymbol{V}(\Omega)\,. \end{aligned}} \tag{11}$$

Here, $\mathcal{B}^0:\boldsymbol{H}^1(\Omega)\times\boldsymbol{H}^1(\Omega)\mapsto\mathbb{R}$ is the bilinear form characterizing the virtual work and $\mathcal{F}(\cdot)$ is defined as before,

$$\mathcal{B}^0(\boldsymbol{u}^0,\boldsymbol{v}) = \int_\Omega \nabla\boldsymbol{v}:\boldsymbol{E}^0\nabla\boldsymbol{u}^0\,\mathrm{d}\boldsymbol{x} \qquad \mathcal{F}(\boldsymbol{v}) = \int_\Omega \boldsymbol{f}\cdot\boldsymbol{v}\,\mathrm{d}\boldsymbol{x} + \int_{\Gamma_t}\boldsymbol{t}\cdot\boldsymbol{v}\,\mathrm{d}s\,. \tag{12}$$

In usual engineering calculations, $\boldsymbol{E}^0$ is a constant function in $[L^\infty(\Omega)]^{N^2\times N^2}$, and $\boldsymbol{E}^0$ satisfies conditions of symmetry and ellipticity: $\exists\alpha^0_\ell$, $\alpha^0_v>0$ such that $\forall\boldsymbol{A}\in\mathbb{R}^{N\times N}$, $\boldsymbol{A}=\boldsymbol{A}^{\mathrm{T}}$ (a.e. $\boldsymbol{x}\in\bar{\Omega}$),

$$\boxed{\begin{aligned} &\alpha^0_v\boldsymbol{A}:\boldsymbol{A}\geqslant\boldsymbol{A}:\boldsymbol{E}^0(\boldsymbol{x})\boldsymbol{A}\geqslant\alpha^0_\ell\boldsymbol{A}:\boldsymbol{A} \\ &E^0_{ijkl}(\boldsymbol{x}) = E^0_{jikl}(\boldsymbol{x}) = E^0_{ijlk}(\boldsymbol{x}) = E^0_{klij}(\boldsymbol{x}) \quad 1\leqslant i,j,k,l\leqslant N\,, \end{aligned}} \tag{13}$$

where E^0_{ijkl} are Cartesian components of $\boldsymbol{E}^0$. The boundary conditions are identical to those of the

heterogeneous problem. Under the adopted conditions both (7) and (11) possess unique solutions $\boldsymbol{u}$, $\boldsymbol{u}^0 \in \{\hat{\boldsymbol{u}}\} + \boldsymbol{V}(\Omega)$, respectively.

The fine-scale energy norm of functions $\boldsymbol{v} \in \boldsymbol{H}^1(\Omega)$ is defined by

$$\|\boldsymbol{v}\|^2_{E(\Omega)} = \mathcal{B}(\boldsymbol{v}, \boldsymbol{v}) = \int_\Omega \nabla \boldsymbol{v} : \boldsymbol{E} \nabla \boldsymbol{v} \, \mathrm{d}\boldsymbol{x} \,, \tag{14}$$

where the actual elasticity tensor $\boldsymbol{E}$ is used.

2.3. Components of the error

In this paper, we shall make the natural choice, $\|\boldsymbol{u} - \boldsymbol{u}^0\|_{E(\Omega)}$, as the measure of the error between the finest and coarsest scales. In general, even the exact solution $\boldsymbol{u}^0$ cannot be obtained analytically and a finite dimensional approximation to it must be used; for example, a finite element approximation $\boldsymbol{u}^{0,h}$. Directly by the triangle inequality,

$$\|\boldsymbol{u} - \boldsymbol{u}^{0,h}\|_{E(\Omega)} \leq \underbrace{\|\boldsymbol{u} - \boldsymbol{u}^0\|_{E(\Omega)}}_{\text{Modeling error}} + \underbrace{\|\boldsymbol{u}^0 - \boldsymbol{u}^{0,h}\|_{E(\Omega)}}_{\text{Numerical error}} \,. \tag{15}$$

Therefore, *two* sources of error occur in approximation of the heterogeneous problem, a *modeling* error, due to the selection of homogenized properties and a *discretization* error inherent in the finite dimensional approximation of the homogenized problem. Discussion of the numerical error characterization, which is not the subject of this paper, can be found in standard texts (see [10]). The remainder of the paper is concerned with the modeling error and its use in characterizing the material response.

3. Modelling error: The relationship between scales

3.1. Explicit a posteriori bounds on the modeling error

Key to the ability to assess the quality of the homogenized solution generated by using $\boldsymbol{E}^0$, is the development of an accurate error estimate which is independent of the loading and boundary conditions. In this section we develop an explicit expression for the difference of the fine-scale and coarse-scale solutions in the fine-scale energy norm, $\|\boldsymbol{u} - \boldsymbol{u}^0\|_{E(\Omega)}$. We first record some properties of the elasticity operator $\boldsymbol{E} \in [L^\infty(\Omega)]^{N^2 \times N^2}$ viewed as an $\boldsymbol{L}^2(\Omega)$-map. Let

$$\boldsymbol{L}^2_{\mathrm{sym}}(\Omega) = \{\boldsymbol{A} \in [L^2(\Omega)]^{N \times N}; \boldsymbol{A}^{\mathrm{T}} = \boldsymbol{A}\} \,, \tag{16}$$

and denote the L^2-inner product and norm on $\boldsymbol{L}^2_{\mathrm{sym}}(\Omega)$ by

$$((\boldsymbol{A}, \boldsymbol{B})) = \int_\Omega \boldsymbol{A} : \boldsymbol{B} \, \mathrm{d}\boldsymbol{x} \qquad |||\boldsymbol{A}|||^2 = ((\boldsymbol{A}, \boldsymbol{A})) \,. \tag{17}$$

The operator $\boldsymbol{E} : \boldsymbol{L}^2_{\mathrm{sym}}(\Omega) \mapsto \boldsymbol{L}^2_{\mathrm{sym}}(\Omega)$ is a self-adjoint, positive definite operator:

$$((\boldsymbol{EA}, \boldsymbol{A})) > 0 \quad \forall \boldsymbol{A} \in \boldsymbol{L}^2_{\mathrm{sym}}(\Omega) \,, \quad \boldsymbol{A} \neq \boldsymbol{0} \,, \tag{18}$$

$$((\boldsymbol{EA}, \boldsymbol{B})) = ((\boldsymbol{A}, \boldsymbol{EB})) \quad \forall \boldsymbol{A}, \boldsymbol{B} \in \boldsymbol{L}^2_{\mathrm{sym}}(\Omega) \,. \tag{19}$$

It is well known that for such operators, the 'square-root' is well defined, generally in terms of the eigenvalue of $\boldsymbol{E}$, and

$$((\boldsymbol{EA}, \boldsymbol{B})) = ((\boldsymbol{E}^{1/2}\boldsymbol{A}, \boldsymbol{E}^{1/2}\boldsymbol{B})) \quad \text{and} \quad |||\boldsymbol{A}|||^2_{E(\Omega)} = ((\boldsymbol{E}^{1/2}\boldsymbol{A}, \boldsymbol{E}^{1/2}\boldsymbol{A})) \,. \tag{20}$$

Using this notation, it is readily verified that

$$\mathcal{B}(\boldsymbol{u}, \boldsymbol{v}) = \int_\Omega \nabla \boldsymbol{u} : \boldsymbol{E} \nabla \boldsymbol{v} \, \mathrm{d}\boldsymbol{x} = ((\boldsymbol{E}^{1/2}\nabla \boldsymbol{u}, \boldsymbol{E}^{1/2}\nabla \boldsymbol{v})) \quad \forall \boldsymbol{u}, \boldsymbol{v} \in \boldsymbol{V}(\Omega) \,, \tag{21}$$

so that

$$\|\boldsymbol{v}\|^2_{E(\Omega)} = \mathscr{B}(\boldsymbol{v}, \boldsymbol{v}) = ((\boldsymbol{E}^{1/2}\nabla\boldsymbol{v}, \boldsymbol{E}^{1/2}\nabla\boldsymbol{v})) \,. \tag{22}$$

With the previous definitions in place, we establish the following error bound.

THEOREM 3.1.1. Let $\boldsymbol{E}$ be a tensor-valued function in $[L^\infty(\Omega)]^{N^2\times N^2}$ satisfying (10) and let $\boldsymbol{E}^0$ be a tensor satisfying (13). Let $\boldsymbol{u}$ and $\boldsymbol{u}^0$ be the corresponding solutions to boundary value problems (7) and (11), respectively. Then

$$\|\boldsymbol{u} - \boldsymbol{u}^0\|_{E(\Omega)} \leq |||\mathscr{J}_0\nabla\boldsymbol{u}^0|||_{E(\Omega)} \quad \mathscr{J}_0 = \boldsymbol{I} - \boldsymbol{E}^{-1}\boldsymbol{E}^0 \,, \tag{23}$$

where explicitly

$$|||\mathscr{J}_0\nabla\boldsymbol{u}^0|||^2_{E(\Omega)} = \int_\Omega (\boldsymbol{I} - \boldsymbol{E}^{-1}\boldsymbol{E}^0)\nabla\boldsymbol{u}^0 : \boldsymbol{E}(\boldsymbol{I} - \boldsymbol{E}^{-1}\boldsymbol{E}^0)\nabla\boldsymbol{u}^0 \, \mathrm{d}\boldsymbol{x} \,. \tag{24}$$

PROOF. Denote by $\Delta\mathscr{B}(\cdot,\cdot)$, the difference, for arbitrary $\boldsymbol{v}\in\boldsymbol{V}(\Omega)$,

$$\Delta\mathscr{B}^0(\boldsymbol{u}^0, \boldsymbol{v}) = \mathscr{B}(\boldsymbol{u}^0, \boldsymbol{v}) - \mathscr{B}^0(\boldsymbol{u}^0, \boldsymbol{v}) = \int_\Omega \nabla\boldsymbol{v} : (\boldsymbol{E} - \boldsymbol{E}^0)\nabla\boldsymbol{u}^0 \, \mathrm{d}\boldsymbol{x} \,. \tag{25}$$

Substituting (25) into (11) gives

$$\mathscr{B}(\boldsymbol{u}^0, \boldsymbol{v}) - \Delta\mathscr{B}^0(\boldsymbol{u}^0, \boldsymbol{v}) = \mathscr{F}(\boldsymbol{v}) = \mathscr{B}(\boldsymbol{u}, \boldsymbol{v}) \,, \tag{26}$$

which directly leads to

$$\mathscr{B}(\boldsymbol{u} - \boldsymbol{u}^0, \boldsymbol{v}) = -\Delta\mathscr{B}^0(\boldsymbol{u}^0, \boldsymbol{v}) = -((\nabla\boldsymbol{v}, (\boldsymbol{E} - \boldsymbol{E}^0)\nabla\boldsymbol{u}^0)) \quad \forall\, \boldsymbol{v}\in\boldsymbol{V}(\Omega) \,. \tag{27}$$

Setting $\boldsymbol{v} = \boldsymbol{u} - \boldsymbol{u}^0$, gives

$$\begin{aligned}
\|\boldsymbol{u} - \boldsymbol{u}^0\|^2_{E(\Omega)} &= -((\nabla(\boldsymbol{u} - \boldsymbol{u}^0), (\boldsymbol{E} - \boldsymbol{E}^0)\nabla\boldsymbol{u}^0)) \\
&= -((\nabla(\boldsymbol{u} - \boldsymbol{u}^0), \boldsymbol{E}\boldsymbol{E}^{-1}(\boldsymbol{E} - \boldsymbol{E}^0)\nabla\boldsymbol{u}^0)) \\
&= -(\boldsymbol{E}^{1/2}\nabla(\boldsymbol{u} - \boldsymbol{u}^0), \boldsymbol{E}^{1/2}\boldsymbol{E}^{-1}(\boldsymbol{E} - \boldsymbol{E}^0)\nabla\boldsymbol{u}^0)) \\
&= -(\boldsymbol{E}^{1/2}\nabla(\boldsymbol{u} - \boldsymbol{u}^0), \boldsymbol{E}^{1/2}\mathscr{J}_0\nabla\boldsymbol{u}^0)) \\
&\leq [((\boldsymbol{E}^{1/2}\nabla(\boldsymbol{u} - \boldsymbol{u}^0), \boldsymbol{E}^{1/2}\nabla(\boldsymbol{u} - \boldsymbol{u}^0)))]^{1/2}[((\boldsymbol{E}^{1/2}\mathscr{J}_0\nabla\boldsymbol{u}^0, \boldsymbol{E}^{1/2}\mathscr{J}_0\nabla\boldsymbol{u}^0))]^{1/2} \\
&= \|\boldsymbol{u} - \boldsymbol{u}^0\|_{E(\Omega)}|||\mathscr{J}_0\nabla\boldsymbol{u}^0|||_{E(\Omega)} \,,
\end{aligned} \tag{28}$$

from which the assertion follows. □

3.1.1. Observations

In Theorem 3.1, the proof makes use of the fact that the coarse-scale solution satisfies a global variational statement, with the same boundary conditions as the fine-scale formulation. If we replace $\boldsymbol{E}^0$ by $\boldsymbol{E}^M$ and, correspondingly, $\boldsymbol{u}^0$ by $\boldsymbol{u}^M$, where $\boldsymbol{E}^M$ is not necessarily constant, then we immediately obtain the following:

$$\|\boldsymbol{u} - \boldsymbol{u}^M\|_{E(\Omega)} \leq |||\mathscr{J}_M\nabla\boldsymbol{u}^M|||_{E(\Omega)} \qquad \mathscr{J}_M = \boldsymbol{I} - \boldsymbol{E}^{-1}\boldsymbol{E}^M \,. \tag{29}$$

This result proves to be useful in later analyses. An algorithm for construction of sequences of material tensors $\boldsymbol{E}^M$ is given in Section 5.

3.2. Connection with classical bounds

Now we establish a connection between the presented error bound and classical bounds for the overall elasticity tensor (see [6] for details). This tensor is defined by the relation

$$\langle\boldsymbol{\sigma}\rangle = \boldsymbol{E}^*\langle\boldsymbol{\epsilon}\rangle \qquad \boldsymbol{\sigma} = \boldsymbol{E}\boldsymbol{\epsilon} \qquad \boldsymbol{\epsilon} = \{\nabla\boldsymbol{u} + (\nabla\boldsymbol{u})^{\mathrm{T}}\}/2 \,, \tag{30}$$

where $\langle\cdot\rangle = 1/|\Omega| \int_\Omega \cdot \, d\boldsymbol{x}$. In general, $\boldsymbol{E}^*$ is not a material property, i.e. it depends on the data. If $\langle\boldsymbol{\sigma}\rangle$ and $\langle\boldsymbol{\epsilon}\rangle$ are such that

$$\langle\boldsymbol{\sigma}\cdot\boldsymbol{\epsilon}\rangle = \langle\boldsymbol{\sigma}\rangle\cdot\langle\boldsymbol{\epsilon}\rangle \tag{31}$$

and $\boldsymbol{f} = \boldsymbol{0}$, then there exist universal bounds for the eigenvalues of $\boldsymbol{E}^*$. This restriction, often referred to in the literature as Hill's condition, can be realized in several ways [5,7]. The bounds for $\boldsymbol{E}^*$ are given by

$$\langle\boldsymbol{E}^{-1}\rangle^{-1} \leqslant \boldsymbol{E}^* \leqslant \langle\boldsymbol{E}\rangle \, . \tag{32}$$

This inequality means that the eigenvalues of the tensors $\boldsymbol{E}^* - \langle\boldsymbol{E}^{-1}\rangle^{-1}$ and $\langle\boldsymbol{E}\rangle - \boldsymbol{E}^*$ are non-negative.

A special class of fields that fall under Hill's condition (31) are those produced in bodies with specified boundary data of the following form: (1) pure displacements in the form $\boldsymbol{u} = \mathcal{S}\cdot\boldsymbol{x}$ or (2) pure tractions in the form $\boldsymbol{t} = \mathcal{T}\cdot\boldsymbol{n}$; where the tensors $\mathcal{S}$ and $\mathcal{T}$ are constant strain and stress tensors, respectively. It can be easily shown that under uniform conditions with no body forces, that for case (1): $\langle\boldsymbol{\epsilon}\rangle = \mathcal{S}$, and for case (2): $\langle\boldsymbol{\sigma}\rangle = \mathcal{T}$. These boundary conditions are referred to as uniform for obvious reasons. If we restrict our attention to uniform boundary conditions, the general error bounds take on special forms. We have the following (with $\boldsymbol{E}^0$ constant),

$$\begin{aligned}
\|\boldsymbol{u} - \boldsymbol{u}^0\|^2_{E(\Omega)} &\leqslant \int_\Omega (\boldsymbol{I} - \boldsymbol{E}^{-1}\boldsymbol{E}^0)\nabla\boldsymbol{u}^0 : \boldsymbol{E}(\boldsymbol{I} - \boldsymbol{E}^{-1}\boldsymbol{E}^0)\nabla\boldsymbol{u}^0 \, d\boldsymbol{x} \\
&= \int_\Omega (\nabla\boldsymbol{u}^0 - \boldsymbol{E}^{-1}\boldsymbol{E}^0\nabla\boldsymbol{u}^0) : (\boldsymbol{E}\nabla\boldsymbol{u}^0 - \boldsymbol{E}^0\nabla\boldsymbol{u}^0) \, d\boldsymbol{x} \\
&= \int_\Omega (\nabla\boldsymbol{u}^0 : \boldsymbol{E}\nabla\boldsymbol{u}^0 - \nabla\boldsymbol{u}^0 : \boldsymbol{E}^0\nabla\boldsymbol{u}^0 - \boldsymbol{E}^{-1}\boldsymbol{E}^0\nabla\boldsymbol{u}^0 : \boldsymbol{E}\nabla\boldsymbol{u}^0 + \boldsymbol{E}^{-1}\boldsymbol{E}^0\nabla\boldsymbol{u}^0 : \boldsymbol{E}^0\nabla\boldsymbol{u}^0) \, d\boldsymbol{x} \\
&= \nabla\boldsymbol{u}^0 : \langle\boldsymbol{E}\rangle\nabla\boldsymbol{u}^0|\Omega| - \nabla\boldsymbol{u}^0 : \boldsymbol{E}^0\nabla\boldsymbol{u}^0|\Omega| - \boldsymbol{E}^0\nabla\boldsymbol{u}^0 : \nabla\boldsymbol{u}^0|\Omega| + \langle\boldsymbol{E}^{-1}\rangle\boldsymbol{E}^0\nabla\boldsymbol{u}^0 : \boldsymbol{E}^0\nabla\boldsymbol{u}^0|\Omega| \, .
\end{aligned} \tag{33}$$

OBSERVATION 1. For those cases having either type of uniform boundary conditions, with no body forces, it is straightforward to show that if the classical upper bound is chosen, $\boldsymbol{E}^0 = \langle\boldsymbol{E}\rangle$, then

$$\begin{aligned}
&\nabla\boldsymbol{u}^0 : \langle\boldsymbol{E}\rangle\nabla\boldsymbol{u}^0|\Omega| - \nabla\boldsymbol{u}^0 : \boldsymbol{E}^0\nabla\boldsymbol{u}^0|\Omega| - \boldsymbol{E}^0\nabla\boldsymbol{u}^0 : \nabla\boldsymbol{u}^0|\Omega| + \langle\boldsymbol{E}^{-1}\rangle\boldsymbol{E}^0\nabla\boldsymbol{u}^0 : \boldsymbol{E}^0\nabla\boldsymbol{u}^0|\Omega| \\
&= 0 - \boldsymbol{E}^0\nabla\boldsymbol{u}^0 : \nabla\boldsymbol{u}^0|\Omega| + \langle\boldsymbol{E}^{-1}\rangle\boldsymbol{E}^0\nabla\boldsymbol{u}^0 : \boldsymbol{E}^0\nabla\boldsymbol{u}^0|\Omega| \\
&= \boldsymbol{E}^0\nabla\boldsymbol{u}^0 : \{-\boldsymbol{I} + \langle\boldsymbol{E}^{-1}\rangle\langle\boldsymbol{E}\rangle\}\nabla\boldsymbol{u}^0|\Omega| \\
&= \langle\boldsymbol{E}\rangle\nabla\boldsymbol{u}^0 : \{-\langle\boldsymbol{E}\rangle^{-1} + \langle\boldsymbol{E}^{-1}\rangle\}\langle\boldsymbol{E}\rangle\nabla\boldsymbol{u}^0|\Omega| \\
&= \boldsymbol{\sigma}^0 : \{-\langle\boldsymbol{E}\rangle^{-1} + \langle\boldsymbol{E}^{-1}\rangle\}\boldsymbol{\sigma}^0|\Omega| \, ,
\end{aligned} \tag{34}$$

where $\boldsymbol{\sigma}^0 (= \boldsymbol{E}^0\boldsymbol{\epsilon}^0)$ is the state of stress that exists in the uniform body. Therefore

$$\|\boldsymbol{u} - \boldsymbol{u}^0\|^2_{E(\Omega)} \leqslant \{-\langle\boldsymbol{E}\rangle^{-1} + \langle\boldsymbol{E}^{-1}\rangle\}\boldsymbol{\sigma}^0 : \boldsymbol{\sigma}^0|\Omega| \, . \tag{35}$$

If the lower bound is chosen: $\boldsymbol{E}^0 = \langle\boldsymbol{E}^{-1}\rangle^{-1}$, then for either type of uniform boundary condition

$$\begin{aligned}
&\nabla\boldsymbol{u}^0 : \langle\boldsymbol{E}\rangle\nabla\boldsymbol{u}^0|\Omega| - \nabla\boldsymbol{u}^0 : \boldsymbol{E}^0\nabla\boldsymbol{u}^0|\Omega| - \boldsymbol{E}^0\nabla\boldsymbol{u}^0 : \nabla\boldsymbol{u}^0|\Omega| + \langle\boldsymbol{E}^{-1}\rangle\boldsymbol{E}^0\nabla\boldsymbol{u}^0 : \boldsymbol{E}^0\nabla\boldsymbol{u}^0|\Omega| \\
&= \nabla\boldsymbol{u}^0 : \langle\boldsymbol{E}\rangle\nabla\boldsymbol{u}^0|\Omega| - \nabla\boldsymbol{u}^0 : \langle\boldsymbol{E}^{-1}\rangle^{-1}\nabla\boldsymbol{u}^0|\Omega| + 0 \\
&= \{\langle\boldsymbol{E}\rangle - \langle\boldsymbol{E}^{-1}\rangle^{-1}\}\nabla\boldsymbol{u}^0 : \nabla\boldsymbol{u}^0|\Omega| \, .
\end{aligned} \tag{36}$$

Therefore,

$$\|\boldsymbol{u} - \boldsymbol{u}^0\|^2_{E(\Omega)} \leqslant \{\langle\boldsymbol{E}\rangle - \langle\boldsymbol{E}^{-1}\rangle^{-1}\}\boldsymbol{\epsilon}^0 : \boldsymbol{\epsilon}^0|\Omega| \, , \tag{37}$$

where $\boldsymbol{\epsilon}^0 (= \boldsymbol{E}^{0-1}\boldsymbol{\sigma}^0)$ is the state of strain that exists in the homogenized body. We observe that in both

of these cases the difference in the classical bounds in (32) appear in the expressions for the modeling error estimates.

OBSERVATION 2. It is straightforward to show that for the uniform displacement case, $\boldsymbol{u} = \mathscr{S} \cdot \boldsymbol{x}$, where $\mathscr{S}$ is arbitrary, that

$$\begin{aligned}\|\boldsymbol{u} - \boldsymbol{u}^0\|^2_{E(\Omega)} &= \int_\Omega \nabla \boldsymbol{u} : \boldsymbol{E} \nabla \boldsymbol{u} \, \mathrm{d}\boldsymbol{x} + \nabla \boldsymbol{u}^0 : \boldsymbol{E}^0 \nabla \boldsymbol{u}^0 |\Omega| - 2 \int_\Omega \nabla \boldsymbol{u}^0 : \boldsymbol{E} \nabla \boldsymbol{u} \, \mathrm{d}\boldsymbol{x} \\ &= \langle \boldsymbol{\epsilon} \rangle : \langle \boldsymbol{\sigma} \rangle |\Omega| + \nabla \boldsymbol{u}^0 : \boldsymbol{E}^0 \nabla \boldsymbol{u}^0 |\Omega| - 2 \boldsymbol{\epsilon}^0 : \langle \boldsymbol{\sigma} \rangle |\Omega| \\ &= \{ \langle \boldsymbol{E} \rangle - \boldsymbol{E}^* \} \mathscr{S} : \mathscr{S} |\Omega| \leq \{ \langle \boldsymbol{E} \rangle - \langle \boldsymbol{E}^{-1} \rangle^{-1} \} \mathscr{S} : \mathscr{S} |\Omega| \,, \end{aligned} \tag{38}$$

where $\boldsymbol{E}^{*-1} \langle \boldsymbol{\sigma} \rangle = \langle \boldsymbol{\epsilon} \rangle = \boldsymbol{\epsilon}^0 = \mathscr{S}$. The last term on the right in (38) is a universal bound, i.e. it is independent of the microstructure. Also, it is easy to show that for the uniform traction case, $\boldsymbol{t} = \mathscr{T} \cdot \boldsymbol{n}$, where $\mathscr{T}$ is arbitrary that

$$\begin{aligned}\|\boldsymbol{u} - \boldsymbol{u}^0\|^2_{E(\Omega)} &= \int_\Omega \nabla \boldsymbol{u} : \boldsymbol{E} \nabla \boldsymbol{u} \, \mathrm{d}\boldsymbol{x} + \nabla \boldsymbol{u}^0 : \boldsymbol{E}^0 \nabla \boldsymbol{u}^0 |\Omega| - 2 \int_\Omega \nabla \boldsymbol{u}^0 : \boldsymbol{E} \nabla \boldsymbol{u} \, \mathrm{d}\boldsymbol{x} \\ &= \langle \boldsymbol{\epsilon} \rangle : \langle \boldsymbol{\sigma} \rangle |\Omega| + \nabla \boldsymbol{u}^0 : \boldsymbol{E}^0 \nabla \boldsymbol{u}^0 |\Omega| - 2 \boldsymbol{\epsilon}^0 : \langle \boldsymbol{\sigma} \rangle |\Omega| \\ &= \boldsymbol{E}^{*-1} \langle \boldsymbol{\sigma} \rangle : \langle \boldsymbol{\sigma} \rangle |\Omega| + \nabla \boldsymbol{u}^0 : \boldsymbol{E}^0 \nabla \boldsymbol{u}^0 |\Omega| - 2 \boldsymbol{\epsilon}^0 : \langle \boldsymbol{\sigma} \rangle |\Omega| \\ &= \boldsymbol{E}^{*-1} \mathscr{T} : \mathscr{T} |\Omega| + \nabla \boldsymbol{u}^0 : \boldsymbol{E}^0 \nabla \boldsymbol{u}^0 |\Omega| - 2 \boldsymbol{\epsilon}^0 : \mathscr{T} |\Omega| \,. \end{aligned} \tag{39}$$

It is easy to show with $\boldsymbol{E}^0 = \langle \boldsymbol{E} \rangle$, that $\boldsymbol{E}^{*-1} \mathscr{T} : \mathscr{T} |\Omega| + \nabla \boldsymbol{u}^0 : \boldsymbol{E}^0 \nabla \boldsymbol{u}^0 |\Omega| - 2 \boldsymbol{\epsilon}^0 : \mathscr{T} |\Omega|$ is a minimum. Therefore

$$\begin{aligned}\|\boldsymbol{u} - \boldsymbol{u}^0\|^2_{E(\Omega)} &= \boldsymbol{E}^{*-1} \mathscr{T} : \mathscr{T} |\Omega| + \nabla \boldsymbol{u}^0 : \boldsymbol{E}^0 \nabla \boldsymbol{u}^0 |\Omega| - 2 \boldsymbol{\epsilon}^0 : \mathscr{T} |\Omega| \\ &= \boldsymbol{E}^{*-1} \mathscr{T} : \mathscr{T} |\Omega| + \nabla \boldsymbol{u}^0 : \boldsymbol{E}^0 \nabla \boldsymbol{u}^0 |\Omega| - 2 \boldsymbol{\epsilon}^0 : \mathscr{T} |\Omega| \\ &= \{ \langle \boldsymbol{E} \rangle \boldsymbol{E}^{*-1} \langle \boldsymbol{E} \rangle - \langle \boldsymbol{E} \rangle \} \boldsymbol{\epsilon}^0 : \boldsymbol{\epsilon}^0 |\Omega| \\ &\leq \{ \langle \boldsymbol{E} \rangle \langle \boldsymbol{E}^{-1} \rangle \langle \boldsymbol{E} \rangle - \langle \boldsymbol{E} \rangle \} \boldsymbol{\epsilon}^0 : \boldsymbol{\epsilon}^0 |\Omega| \,, \end{aligned} \tag{40}$$

where $\boldsymbol{E}^* \langle \boldsymbol{\epsilon} \rangle = \langle \boldsymbol{\sigma} \rangle = \boldsymbol{\sigma}^0 = \mathscr{T} = \boldsymbol{E}^0 \boldsymbol{\epsilon}^0$. The last term on the right in (40) is a minimum universal upper bound. The two universal bounding materials in the previous cases have the following ordering:

$$\{ \langle \boldsymbol{E} \rangle - \boldsymbol{E}^* \} \leq \{ \langle \boldsymbol{E} \rangle - \langle \boldsymbol{E}^{-1} \rangle^{-1} \} \leq \{ \langle \boldsymbol{E} \rangle \langle \boldsymbol{E}^{-1} \rangle \langle \boldsymbol{E} \rangle - \langle \boldsymbol{E} \rangle \} \,. \tag{41}$$

In the next section we conduct numerical experiments on the global and local estimation of the modeling error with body forces and non-uniform boundary conditions in place.

4. Numerical experiments on error estimation

4.1. Example 1: A heterogeneous bar

To eliminate any effect of numerical error on the study of the error bound, we first consider an example with an analytical solution. To this end, we consider a linear elastic rod, of unit length, fixed on both ends, and subject to a constant body force (see the top three diagrams in Fig. 7). The fine-scale and homogenized problems are

$$\frac{\mathrm{d}}{\mathrm{d}x} \left(E(x) \frac{\mathrm{d}u(x)}{\mathrm{d}x} \right) = -1 \,, \qquad u(0) = 0 \,, \qquad u(1) = 0 \tag{42}$$

and

$$\frac{\mathrm{d}}{\mathrm{d}x} \left(E^0 \frac{\mathrm{d}u^0(x)}{\mathrm{d}x} \right) = -1 \,, \qquad u^0(0) = 0 \,, \qquad u^0(1) = 0 \,. \tag{43}$$

Here, our interest is to determine performance of the error bound (23) in predicting global and local modeling error throughout the body. To this end, for local resolution of the error we let $\mathcal{Q}$ denote an arbitrary partition of Ω with a total number of subdomains, $N = N(\mathcal{Q})$, such that

$$\bar{\Omega} = \bigcup_{K=0}^{N(\mathcal{Q})} \bar{\Theta}_K \quad \Theta_K, \Theta_L \in \mathcal{Q} \quad \Theta_K \cap \Theta_L = \emptyset \quad \text{if } K \neq L \quad 1 \leq K, L \leq N(\mathcal{Q}) . \tag{44}$$

We define local error indicators, local measures of the error, for $\Theta_K \subset \Omega$ by

$$\zeta_K = |||\mathcal{I}_0 \nabla \boldsymbol{u}^0||_{t_{E(\Theta_K)}} \qquad 1 \leq K \leq N(\mathcal{Q}) . \tag{45}$$

For the global error estimator we simply take the global error bound $\zeta = |||\mathcal{I}_0 \nabla \boldsymbol{u}^0|||_{E(\Omega)}$. Clearly

$$\|\boldsymbol{u} - \boldsymbol{u}^0\|^2_{E(\Omega)} \leq \sum_{K=1}^{N(\mathcal{Q})} (\zeta_K)^2 . \tag{46}$$

The quality of the global and local error indicators is measured by effectivity indices η and η_K, respectively:

$$\eta_K = \frac{\zeta_K}{\|\boldsymbol{u} - \boldsymbol{u}^0\|_{E(\Theta_K)}} \qquad \eta^2 = \sum_{K=1}^{N(\mathcal{Q})} \eta_K^2 . \tag{47}$$

In our example, the unit interval is divided into 10 000 equal intervals, and for each interval the material property is chosen at random to be either $E = 1$ or $E = \tau$, where τ is the mismatch ratio. Equal amounts of hard and soft material are used. A coarser partition is overlaid representing the subdomain partition. The following tests are entirely representative of many realizations of the interval and subdomain partitioning for this simple one-dimensional case. All of the following calculations are done *analytically*. For convenience, and to illustrate the sensitivity of the results to the choice of $\boldsymbol{E}^0$, we choose the classical upper and lower bounds in (32). Our objective is to illustrate the dependence of the effectivity indices on the domain partitioning and the choice of $\boldsymbol{E}^0$.

4.1.1. Results

From Tables 1 and 2, it is seen that an increase in the number of subdomains in the partition reduces the quality of the local effectivity indices. This stems from the fact that the local estimates are derived from a global calculation that, due to its integral nature, is insensitive to local pointwise information. The local effectivity indices are closely clustered around unity for the harmonic average, independent of the mismatch, while this is not the case for the arithmetic average. Locally, the error indicators are not guaranteed to be upper bounds on the error, and, as Tables 1 and 2 show, they underestimate the error in some parts of the domain. The choice of homogenization affects the quality of the local estimates,

Table 1
The effectivity indices for $\boldsymbol{E}^0 = \langle \boldsymbol{E} \rangle$ for 100 subdomains and 10 subdomains, versus mismatch ratio

τ	$\|\boldsymbol{u} - \boldsymbol{u}^0\|_{E(\Omega)} / \|\boldsymbol{u}\|_{E(\Omega)}$	η	$\max \eta_K$ $N = 100, 10$		$\min \eta_K$ $N = 100, 10$	
10	0.804457	1.000186	1.38345	1.06948	0.529439	0.93348
50	0.956960	1.000205	1.66329	1.09153	0.494427	0.91889
100	0.978203	1.000208	1.71799	1.09488	0.489773	0.91681

Table 2
The effectivity indices for $\boldsymbol{E}^0 = \langle \boldsymbol{E}^{-1} \rangle^{-1}$ for 100 subdomains and 10 subdomains, versus mismatch ratio

τ	$\|\boldsymbol{u} - \boldsymbol{u}^0\|_{E(\Omega)} / \|\boldsymbol{u}\|_{E(\Omega)}$	η	$\max \eta_K$ $N = 100, 10$		$\min \eta_K$ $N = 100, 10$	
10	1.347399	1.000066	1.006312	1.000608	0.858558	0.996870
50	3.276713	1.000018	1.001734	1.000158	0.955632	0.999186
100	4.680409	1.000009	1.000906	1.000082	0.976185	0.999578

although this effect is barely perceivable globally. Interestingly, the error prediction for the harmonic average case becomes better with increasing mismatch ratio—*this is strictly an anomaly associated with this specific one-dimensional problem, and, in general, is not necessarily the case*. Note that even for this simple one-dimensional problem, the error for the arithmetic average ranges from 80–90% of the actual solution, and for the harmonic average, 134–468%. It easy to show that, with respect to the energy norm, the arithmetic average is within a fraction of one percent of being the optimal homogenized material choice to minimize the modeling error in energy for this specific problem.

4.2. *Example 2: A three-dimensional analysis of a cube in shear*

We consider a unit cube of material, with a heterogeneous two phase isotropic random 'checkerboard' microstructure (Fig. 1). We choose $\boldsymbol{E}^0$ to be isotropic, where the specific values of the homogenized Lamé parameters are simply the volumetric average of the Lamé parameters of the internal constituents. The unit volume is divided into 64 sub-cubes of equal volume, each with dimensions $1/4 \times 1/4 \times 1/4$. Each sub-cube is randomly assigned, either a set of soft or hard material parameters (Fig. 1)

$$\lambda = \lambda^s \tau \qquad \mu = \mu^s \tau \tag{48}$$

where $\tau \geq 1$ is a constant parameter which represents the mismatch ratio and where λ^s and μ^s are the set of soft Lamé material parameters whose relative ratio, for convenience, is taken to be that of standard grade steel. Equal amounts of hard and soft material are used.

The loading scenario for the heterogeneous cube is shown in Fig. 1. The virtual work formulation for this problem is

Find $\boldsymbol{u}^0 \in \boldsymbol{V}(\Omega)$ such that

$$\int_\Omega \nabla \boldsymbol{v} : \boldsymbol{E}^0 \nabla \boldsymbol{u}^0 \, \mathrm{d}\boldsymbol{x} = \int_{\Gamma_{t_1}} \boldsymbol{t} \cdot \boldsymbol{v} \, \mathrm{d}s \quad \forall \boldsymbol{v} \in \boldsymbol{V}(\Omega) \tag{49}$$

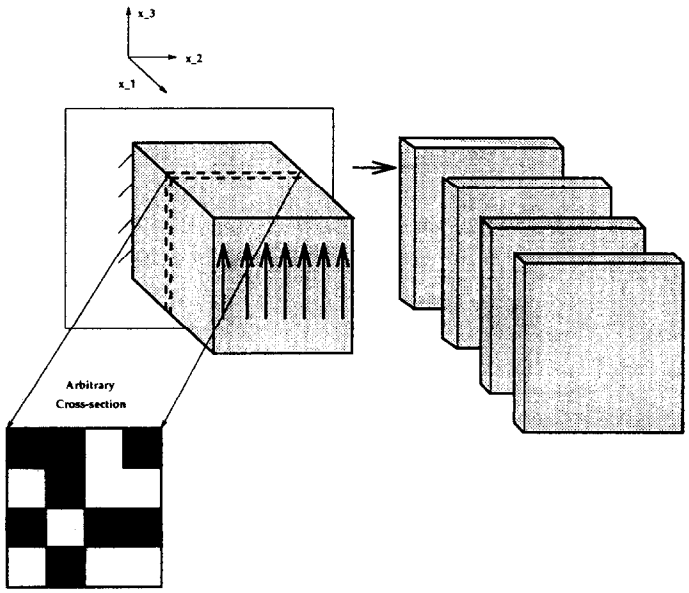

Fig. 1. A test problem for three-dimensional dispersed cuboid microstructure.

where

$$V(\Omega) = \{\boldsymbol{v} \in \boldsymbol{H}^1(\Omega) : \boldsymbol{v}|_{\Gamma_u} = 0\}\ , \tag{50}$$

where

- Ω corresponds to the interior of the $1 \times 1 \times 1$ cube depicted in Fig. 1: $0 < x_1 < 1$, $0 < x_2 < 1$, $0 < x_3 < 1$,
- Γ_u corresponds to the plane $x_1 = 0$,
- Γ_{t_1} corresponds to the plane $x_1 = 1$, where we specify $\boldsymbol{t} = \{0, 0, 1\}^{\mathrm{T}}$ (uniform shear loading),
- $\boldsymbol{f} = \boldsymbol{0}$,
- all other faces of the cube are free surfaces.

For the purposes of numerical experiment, the finite element method is employed to generate approximations to $\boldsymbol{u}$ and $\boldsymbol{u}^0$ denoted by $\boldsymbol{u}^h$ and $\boldsymbol{u}^{0,h}$, respectively. For a measure of the quality of the error prediction locally, we use instead of (47), the local discrete effectivity indices,

$$\eta_K^h = \frac{\zeta_K^h}{\|\boldsymbol{u}^h - \boldsymbol{u}^{0,h}\|_{E(\Theta_K)}} \quad \text{where} \quad \zeta_K^h = |||\mathscr{I}_0 \nabla \boldsymbol{u}^{0,h}|||_{E(\Theta_K)} \quad 1 \leqslant K \leqslant N(\mathscr{Q})\ . \tag{51}$$

In all of the following numerical experiments, the finite element approximation consists of hexahedral elements, with trilinear polynomial interpolation. To illustrate the use of local error indicators, we adopt a simple unidirectional partitioning of the cube into four 'slabs': $\Theta_1 : 0 < x_1 < 1/4$, $\Theta_2 : 1/4 < x_1 < 1/2$, $\Theta_3 : 1/2 < x_1 < 3/4$ and $\Theta_3 : 3/4 < x_1 < 1$. It is clear that the quality of the discrete error indicators is mesh dependent and, consequently, a series of tests are performed to illustrate mesh dependency for fixed mismatch ratios. These tests are conducted in the following manner: keeping the microstructure of the cube fixed, for each sub-cube in the cube, we steadily increase the number of finite elements per sub-cube. In this manner, we isolate the effects of the fineness of the finite element mesh and the mismatch ratio on the discrete effectivity indices.

4.2.1. Results

Tables 3 and 4 contain results which illustrate the behavior of the global and local effectivity indices with increasing finite element mesh refinement for fixed, successively larger mismatches of material properties of 10, 50 and 100. *The actual modeling error varied between a few hundred percent to over 1000%, depending on the mismatch ratio and the finite element mesh.* The effectivity indices, however,

Table 3
The global effectivity indices for mismatch $\tau = 10$, 50, 100 and for increasingly finer finite element meshes

DOF	Elem/sub-cube	η^h, $\tau = 10$, 50, 100
375	$1 \times 1 \times 1$	1.21 1.44 1.52
2187	$2 \times 2 \times 2$	1.34 1.98 2.43
6591	$3 \times 3 \times 3$	1.37 2.15 2.71
14 739	$4 \times 4 \times 4$	1.37 2.15 2.72
27 783	$5 \times 5 \times 5$	1.37 2.14 2.71
46 875	$6 \times 6 \times 6$	1.37 2.14 2.72

Table 4
The local effectivity indices (for each slab) for mismatch $\tau = 10$, 50, 100 and for increasingly finer finite element meshes

DOF	Elem/sub-cube	Slab 1: η_1^h	Slab 2: η_2^h	Slab 3: η_3^h	Slab 4: η_4^h
375	$1 \times 1 \times 1$	1.22 1.46 1.55	0.93 1.05 1.12	1.44 1.67 1.74	1.32 1.66 1.80
2187	$2 \times 2 \times 2$	1.30 1.94 2.41	1.55 2.44 3.08	1.32 1.83 2.45	1.21 1.80 2.45
6591	$3 \times 3 \times 3$	1.57 2.67 3.48	1.29 1.94 2.40	1.29 1.96 2.59	1.35 2.18 2.78
14 739	$4 \times 4 \times 4$	1.43 2.32 2.99	1.27 1.92 2.40	1.30 1.96 2.45	1.51 2.52 3.28
27 783	$5 \times 5 \times 5$	1.31 2.03 2.58	1.39 2.20 2.79	1.41 2.17 2.79	1.38 2.18 2.76
46 875	$6 \times 6 \times 6$	1.36 2.09 2.63	1.37 2.17 2.77	1.35 2.06 2.77	1.40 2.25 2.91

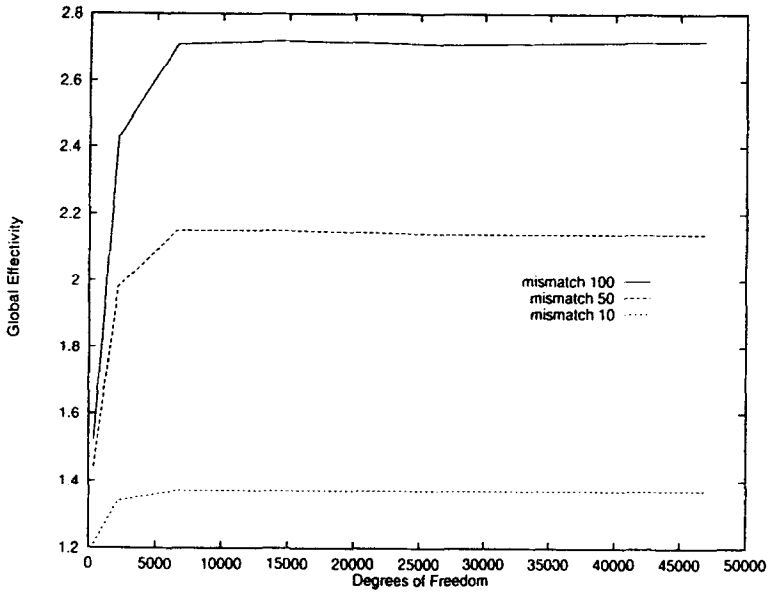

Fig. 2. Behavior of the effectivity index with changes in the number of degrees of freedom, for the cube in shear with cubical microstructure.

are remarkably accurate, which means that we may predict the error well, even though it is quite large. Our global measure of the effectiveness of the error estimate, η^h, is relatively constant after a certain mesh fineness threshold (Fig. 2), which is approximately 27 trilinear hexahedra per sub-cube, and while the local effectivity indices also stabilize, they stabilize at a much slower rate. However, the local effectivity indices are clustered around the global values, suggesting that we may obtain accurate local estimates of the error. We note that the choice of $\boldsymbol{E}^0$ is not restricted to the classical relation of averaged quantities of stress and strain, and that any elasticity that satisfies the ellipticity conditions is admissible. While in practice the exact solution is usually never obtainable, the experiments lend some confidence to the reliability of the estimator. Other loading cases, such as a cantilevered cube in uniaxial tension and a cantilevered cube under the influence of constant body forces, were tested, with qualitatively similar results (not reported here) to the presented shear case.

5. Hierarchical scale construction

In general, the quality of the solution $\boldsymbol{u}^0$ may be poor, even with a good choice of a uniform homogenized description. In order to improve solutions, it is clear that one must develop a method which (efficiently) constructs solution scales between the coarsest-scale, corresponding to a perfectly uniform material description, and the finest-scale. To obtain reasonable accuracy with numerical methods based on discretization, the computational cell size must be less than, or equal to the inhomogeneity sizes encountered in the body. This makes the full fine-scale problem inaccessible, for two main reasons. First, if the full, coupled, fine-scale problem is discretized for an approximate numerical method, it would not fit, due to memory limitations, on existing computers. Second, even if the discrete problem were to fit into a hypothetical 'super-memory' machine, it would take on the order of Cn^2 operations to solve the resulting system, where n is the number of unknowns, and C is a constant, greater than unity and is dependent on the condition number of the resulting discrete stiffness matrix. The value of n is so large (e.g. $n \sim \mathcal{O}(10^7)$) that such computations are not feasible.

To address this difficulty, a series of relatively inexpensive coarse-scale problems are generated, characterized by bodies comprised of subdomains. Each subdomain may contain different constant material properties. The sizes of these subdomains are orders of magnitude larger than the inhomogeneity sizes encountered on the fine-scale (see Fig. 4). These coarser material descriptions form a

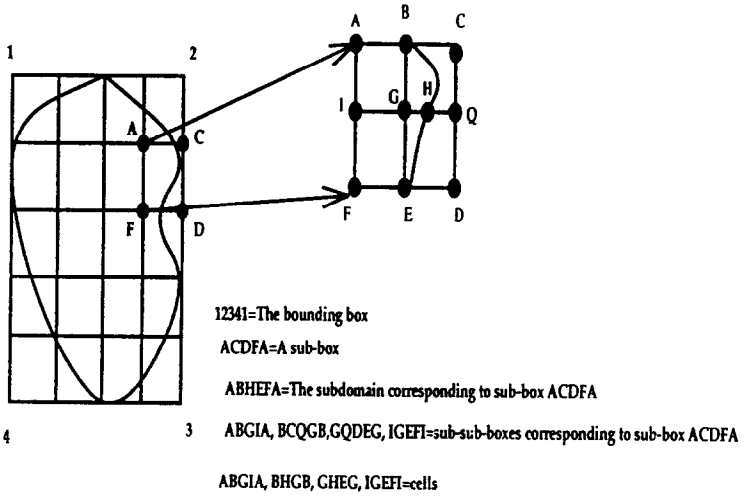

Fig. 3. The nomenclature for the construction of a partition.

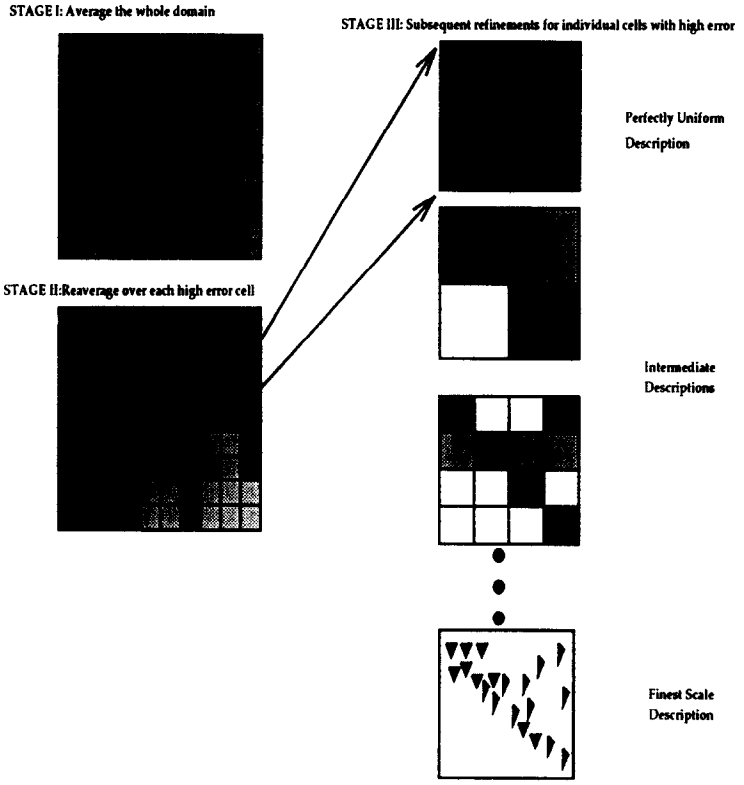

Fig. 4. Hierarchical elasticities produced by ALR for a single Cartesian subdomain.

hierarchical family of scales of material description. The modeling error throughout the body is estimated at each scale, with the error estimator introduced previously, and the material description is refined in those select regions where the modeling error is high. The global coarse-scale problem is then resolved with the new material properties, and the error re-estimated, until a desired prespecified tolerance is met. However, in general, these hierarchical solutions do not capture much of the fine-scale information, and, therefore, a post-processing method is applied which adds a local fine-scale perturbation to the hierarchical solution. This process endows coarse-scale solutions with the necessary information to be reasonably accurate for a local analysis. Therefore, the overall method is comprised of two main stages: (1) generation of hierarchical scales and (2) local solution processes.

5.1. Construction of a partition

Although in the preceding theory the partition for the model error estimation has been based on an arbitrary partition of the domain, in practice, there must be some constraints. For definiteness, we derive a systematic construction which is amenable to numerical computations. We consider a general curvilinear, non-convex domain, and we introduce the idea of a bounding box (Fig. 3). In general, neither the subdomain divisions nor the partitions follow the material boundaries. We define the bounding box, $\square$, as simply an open rectangular parallelpiped such that

$$\text{dia}\square^* = \inf \text{dia}\{\square : \bar{\Omega} \subset \overline{\square}\} . \tag{52}$$

Furthermore, $\square^*$ is subjected to a fixed partition

$$\bigcup_{k=1}^{N} \overline{\square}_K = \overline{\square}^* \quad \square_K \cap \square_L = \emptyset \quad K \neq L \quad 1 \leq K, L \leq N(\mathcal{Q}^{\square}) , \tag{53}$$

where each $\square_K$ is of equal size. We define the subdomain $\Theta_K^{\square} \subset \Omega$ as

$$\Omega \cap \square_K = \Theta_K^{\square} \qquad \bigcup_{K=1}^{N(\mathcal{Q}^{\square})} \overline{\Theta_K^{\square}} = \bar{\Omega} \qquad \Theta_K^{\square} \cap \Theta_L^{\square} = \emptyset \quad K \neq L . \tag{54}$$

We also define partitions within each subdomain $\Theta_K^{\square}$, by first partitioning the corresponding 'sub-boxes' into equal pieces. In one dimension this corresponds to bisecting subdomains into equal line segments, while in two dimensions this corresponds to quadrasecting sub-boxes into equal rectangles, and in three dimensions it corresponds to octasecting sub-boxes into equal hexahedra with rectangular cross-section. We denote these sub-sub-boxes by $\square_{K,L}$, where

$$\bigcup_{L=1}^{N_K} \overline{\square}_{K,L} = \overline{\square}_K \qquad \overline{\square}_{K,L} \subset \overline{\square}_K \qquad \bigcup_{L=1}^{N_K} \overline{\square}_{K,L} = \overline{\square}_K , \tag{55}$$

where N_K is the number of sub-sub-boxes in sub-box K. Furthermore, we define

$$\Omega \cap \square_{K,L} = \Theta_{K,L}^{\square} \tag{56}$$

and clearly

$$\Theta_{K,L}^{\square} \subset \Theta_K^{\square} \qquad \bigcup_{\bar{\Theta}_{K,L}^{\square}} \bar{\Theta}_{K,L}^{\square} = \bar{\Theta}_K^{\square} \tag{57}$$

where $\Theta_{K,L}^{\square}$ are denoted as 'cells' (Fig. 3). It should be clear that sub-box $\square_K$ and $\Theta_K^{\square}$ are identical for Cartesian domains. It is emphasized that the partitions for (1) the error indicators, (2) the hierarchical scale generation and (3) the local post-processing are independent and in practice should be kept independent to obtain maximum performance from the method. However, for clarity of exposition, we use the same partition as for the local error indicators throughout the presentation.

5.2. Stage I: An algorithm for generating hierarchical scales

Overview: A hierarchical family is generated by first starting with a homogeneous material, estimating where the corresponding homogenized solution is in large error, and locally refining of the material description where the error is high. This is an iterative procedure. For clarity of exposition, we illustrate the procedure with isotropic materials and with volumetric averaging for the homogenization process, but neither of these conditions is necessary.

5.2.1. An adaptive algorithm based on Adaptive Local Reaveraging (ALR)

- *Step 0:* Choose an error tolerance: $\|\boldsymbol{u} - \boldsymbol{u}^0\| \leq \delta$ = error tolerance.
- *Step 1:* Solve the initial coarse scale problem, with uniform material properties. For example, suppose $\boldsymbol{E}^0$ is a constant isotropic tensor with material constants,

$$\kappa^0 = \frac{1}{|\Omega|}\int_\Omega \kappa \, dx \qquad \mu^0 = \frac{1}{|\Omega|}\int_\Omega \mu \, dx \,, \tag{58}$$

where, as usual, $\kappa = \lambda + \frac{2}{3}$ denotes the bulk modulus.

- *Step 2:* Distribute the error tolerance in the following fashion,

$$\delta_K = \delta \frac{|\Theta_K^{\square}|}{|\Omega|} \quad \forall\, K = 1, 2, \ldots, N(\mathcal{Q}^{\square}) \tag{59}$$

- *Step 3:* Calculate the following in each subdomain $\Theta_K^{\square}$, $\forall\, K = 1, 2, \ldots, N(\mathcal{Q}^{\square})$,

$$\zeta_K = |||\mathcal{J}_0 \nabla \boldsymbol{u}^0|||_{E(\Theta_K^{\square})} \qquad \mathcal{J}_0 = \boldsymbol{I} - \boldsymbol{E}^{-1}\boldsymbol{E}^0 \,, \tag{60}$$

and check

$$\zeta_K \leqslant \delta_K \quad \forall\, K = 1, 2, \ldots, N(\mathcal{Q}^{\square}) \,. \tag{61}$$

- *Step 4:* If $\zeta_K > \delta_K$, repartition the corresponding sub-box, $\square_K$, into sub-sub-boxes, as given in (55), and generate cells $\Theta_{K,L}^{\square} \subset \Theta_K^{\square}$. Calculate the following for each cell

$$\kappa^1|_{\Theta_{K,L}^{\square}} = \frac{1}{|\Theta_{K,L}^{\square}|}\int_{\Theta_{K,L}^{\square}} \kappa \, dx \qquad \mu^1|_{\Theta_{K,L}^{\square}} = \frac{1}{|\Theta_{K,L}^{\square}|}\int_{\theta_{K,L}^{\square}} \mu \, dx \tag{62}$$

where $|\Theta_{K,L}^{\square}| = \text{meas}(\Theta_{K,L}^{\square})$, and where

$$\boldsymbol{E}^1(\boldsymbol{x})|_{\Theta_{K,L}^{\square}} = \boldsymbol{E}_{K,L}^1 \quad \boldsymbol{x} \in \Theta_{K,L}^{\square} \,. \tag{63}$$

The new material generated by performing one sequence of Steps 1–4 is denoted with superscript 1 as opposed to 0, which was used for the initial data and solution. For example, after completing the first pass of Steps 1–4, the material properties are denoted as κ^1, μ^1 and the corresponding global solution as $\boldsymbol{u}^1$.

- *Step 5:* Repeat Steps 1–4 until the error tolerance has been met. After M stages (Steps 1–4), i.e. after M steps in which at least one sub-box has be repartitioned during a stage, we arrive at a material characterization defined by the tensor $\boldsymbol{E}^M \in [L^\infty(\Omega)]^{N^2 \times N^2}$, such that $\forall\, \boldsymbol{A} \in \mathbb{R}^{N \times N}$, $\boldsymbol{A} = \boldsymbol{A}^{\mathrm{T}}$

$$\boldsymbol{E}^M(\boldsymbol{x})\boldsymbol{A} = \kappa^M(\boldsymbol{x})\frac{1}{3}(\text{tr}\,\boldsymbol{A})\boldsymbol{I} + \mu^M(\boldsymbol{x})\,\text{dev}(\boldsymbol{A}) \quad \text{a.e. } \boldsymbol{x} \in \Omega \tag{64}$$

where $\text{dev}(\boldsymbol{A}) = \boldsymbol{A} - \frac{1}{3}(\text{tr}\,\boldsymbol{A})\boldsymbol{I}$, and where

$$\kappa^M|_{\Theta_{K,L}^{\square}} = \frac{1}{|\Theta_{K,L}^{\square}|}\int_{\Theta_{K,L}^{\square}} \kappa \, dx \qquad \mu^M|_{\Theta_{K,L}^{\square}} = \frac{1}{|\Theta_{K,L}^{\square}|}\int_{\Theta_{K,L}^{\square}} \mu \, dx \,. \tag{65}$$

5.3. Convergence of the ALR solutions

It can be easily shown [8] that the ellipticity constants appearing in (10) are related to κ and μ in the following manner

$$\boxed{\begin{aligned} &0 < \alpha_\ell = \min\{3\kappa, 2\mu\} \\ &\infty > \alpha_v = \max\{3\kappa, 2\mu\} \,. \end{aligned}} \tag{66}$$

Furthermore, we observe that for any $\Theta_{K,L}^{\square} \subset \Omega$,

$$\alpha_\ell \leqslant \frac{1}{|\Theta_{K,L}^{\square}|}\int_{\Theta_{K,L}^{\square}} 3\kappa(\boldsymbol{x})\, dx = \frac{1}{|\Theta_{K,L}^{\square}|}\int_{\Theta_{K,L}^{\square}} 3\lambda(\boldsymbol{x})\, dx + \frac{1}{|\Theta_{K,L}^{\square}|}\int_{\Theta_{K,L}^{\square}} 2\mu(\boldsymbol{x})\, dx \leqslant \alpha_v \,, \tag{67}$$

and

$$\alpha_\ell \leq \frac{1}{|\Theta^{\square}_{K,L}|} \int_{\Theta^{\square}_{K,L}} 2\mu(x)\, dx \leq \alpha_v \,. \tag{68}$$

Therefore, as one would expect,

$$\boxed{\alpha_\ell \leq \{3\kappa^M, 2\mu^M\} \leq \alpha_v \,.} \tag{69}$$

In other words, the material properties of the intermediate scales are bounded by the original ellipticity constants.

THEOREM 5.3.1. Let $\boldsymbol{u}$ *be the solution to (7) and let* $\boldsymbol{u}^M$ *be the solution to the boundary value problem,*

$$\boxed{\begin{aligned} &\text{Find } \boldsymbol{u}^M \in \{\hat{\boldsymbol{u}}\} + V(\Omega) \text{ such that} \\ &\mathcal{B}^M(\boldsymbol{u}^M, \boldsymbol{v}) = \mathcal{F}(\boldsymbol{v}) \quad \forall\, \boldsymbol{v} \in V(\Omega)\,, \end{aligned}} \tag{70}$$

where $\mathcal{B}^M : \boldsymbol{H}^1(\Omega) \times \boldsymbol{H}^1(\Omega) \mapsto \mathbb{R}$ *is the bilinear form characterizing the virtual work for the Mth-stage material,*

$$\mathcal{B}^M(\boldsymbol{u}^M, \boldsymbol{v}) = \int_\Omega \nabla \boldsymbol{v} : \boldsymbol{E}^M \nabla \boldsymbol{u}^M \, dx \tag{71}$$

with $\boldsymbol{E}^M$ *given by (64), and* $\mathcal{F}(\cdot)$ *is defined by (8). Then*

$$\boxed{\|\boldsymbol{u} - \boldsymbol{u}^M\|_{E(\Omega)} \leq \frac{1}{\sqrt{\alpha_\ell}} \|(\boldsymbol{E} - \boldsymbol{E}^M)\nabla \boldsymbol{u}^M\|_{L^2(\Omega)} \,.} \tag{72}$$

PROOF. Let

$$\Delta\mathcal{B}^M(\boldsymbol{u}^M, \boldsymbol{v}) = \mathcal{B}(\boldsymbol{u}^M, \boldsymbol{v}) - \mathcal{B}^M(\boldsymbol{u}^M, \boldsymbol{v}) = \int_\Omega \nabla \boldsymbol{v} : (\boldsymbol{E} - \boldsymbol{E}^M)\nabla \boldsymbol{u}^M \, dx \,. \tag{73}$$

Substituting (73) into the equation associated with (70)

$$\mathcal{B}(\boldsymbol{u}^M, \boldsymbol{v}) - \Delta\mathcal{B}^M(\boldsymbol{u}^M, \boldsymbol{v}) = \mathcal{F}(\boldsymbol{v}) \tag{74}$$

and subtracting the result from (7) yields

$$\mathcal{B}(\boldsymbol{u} - \boldsymbol{u}^M, \boldsymbol{v}) = -\Delta\mathcal{B}^M(\boldsymbol{u}^M, \boldsymbol{v}) \,. \tag{75}$$

Allowing $\boldsymbol{v} = \boldsymbol{u} - \boldsymbol{u}^M$, and by Cauchy–Schwarz

$$\mathcal{B}(\boldsymbol{u} - \boldsymbol{u}^M, \boldsymbol{u} - \boldsymbol{u}^M) \leq \|\nabla(\boldsymbol{u} - \boldsymbol{u}^M)\|_{L^2(\Omega)} \|(\boldsymbol{E} - \boldsymbol{E}^M)\nabla \boldsymbol{u}^M\|_{L^2(\Omega)} \,. \tag{76}$$

Because of the assumed ellipticity of the elasticity tensor (recall (10)),

$$\frac{\|\boldsymbol{u} - \boldsymbol{u}^M\|^2_{E(\Omega)}}{\alpha_\ell} \geq \int_\Omega \nabla(\boldsymbol{u} - \boldsymbol{u}^M) : \nabla(\boldsymbol{u} - \boldsymbol{u}^M) \, dx \,. \tag{77}$$

Therefore

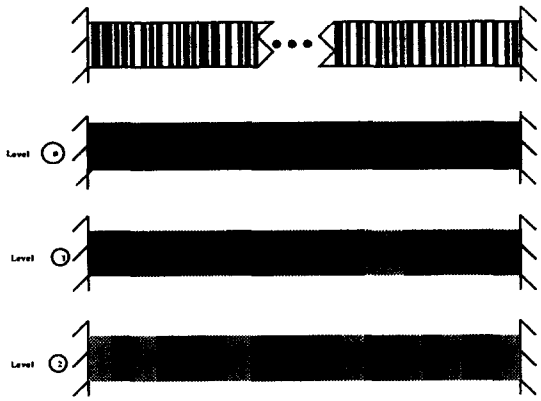

Fig. 5. A hierarchy of scales, for the heterogeneous bar, illustrated for ten subdomains.

$$\|\boldsymbol{u}-\boldsymbol{u}^M\|_{E(\Omega)} \leq \frac{1}{\sqrt{\alpha_\ell}} \|(\boldsymbol{E}-\boldsymbol{E}^M)\nabla \boldsymbol{u}^M\|_{L^2(\Omega)} . \quad \square \tag{78}$$

In general, estimates such as this are asymptotically exact in the sense that as $\boldsymbol{E}^M$ approaches $\boldsymbol{E}$ in $[L^\infty(\Omega)]^{N^2\times N^2}$, as $M\to\infty$, we expect $\boldsymbol{u}^M\to\boldsymbol{u}$ in $V(\Omega)$ by virtue of (72).

5.4. *Stage II: Post-processing the coarse-scale solutions through local fine-scale perturbation*

Overview: While the solutions produced by ALR converge to the fine-scale solution in the energy norm, they may not adequately capture the fine-scale features. Here, we illustrate how the hierarchical solutions can be post-processed in an inexpensive local manner, which is proven to yield superior solutions in an energy sense. The process is as follows: the solution generated by the homogenized material description is used to construct approximate local displacement boundary conditions for interior subdomain boundaries produced by a partition of the problem domain. The exterior boundary conditions are not altered (Fig. 6). The decoupled local problems are then solved. The motivation here is that the detailed solution to several decoupled sub-problems posed on smaller subdomains, are more tractable, and can be computed easily in parallel if desired. The final global solution is then 'reconstructed' by simply reassembling the local solutions, which are conforming. We refer to this procedure as the Homogenized Dirichlet Projection Method, HDPM. The operation counts involved in this

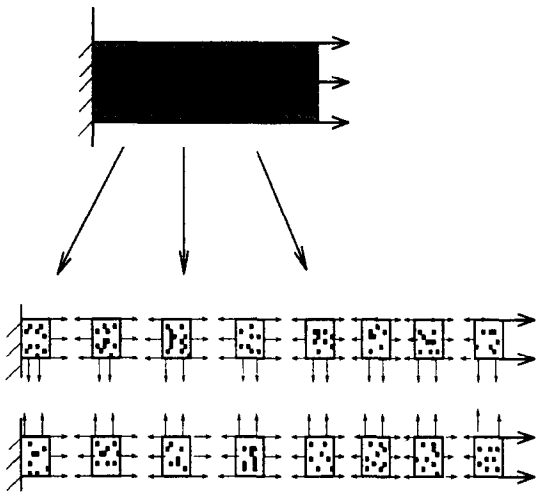

Fig. 6. An example of 'post-processing' or 'decomposition of the domain' or 'local perturbation' using the coarse-scale solution.

procedure are significantly less than those required to solve the hypothetical, coupled, fine-scale problem.

5.5. Construction of local subdomain problems

We define the boundary of an individual subdomain $\Theta_K^{\square}$, as $\partial\Theta_K^{\square}$ consisting of a portion $\Gamma_{\mathbf{Ku}}$ where the displacements are prescribed and a part $\Gamma_{\mathbf{Kt}}$ where tractions are prescribed:

$$\Gamma_{\mathbf{Ku}} = \partial\Theta_K^{\square}\backslash\Gamma_{\mathbf{Kt}} \qquad \Gamma_{\mathbf{Kt}} = \partial\Theta_K^{\square} \cap \Gamma_t \,. \tag{79}$$

We define the following space

$$V(\Theta_K^{\square}) = \{\boldsymbol{v} \in V(\Omega), \boldsymbol{v} = \boldsymbol{0} \text{ on } \Omega\backslash\bar{\Theta}_K^{\square}, \boldsymbol{v}|_{\Gamma_{\mathbf{Ku}}} = 0\} \,. \tag{80}$$

Let $\mathscr{E}_K$, $1 \leq K \leq N(\mathscr{Q}^{\square})$, denote the operator from $V(\Theta_K^{\square})$ into $V(\Omega)$ that identifies each $\boldsymbol{v}_K \in V(\Theta_K^{\square})$ with a function $\boldsymbol{v}$ in $V(\Omega)$ such that

$$\boldsymbol{v}|_{\Theta_K^{\square}} = \boldsymbol{v}_K \qquad \boldsymbol{v}|_{\Omega\backslash\Theta_K^{\square}} = \boldsymbol{0} \,. \tag{81}$$

We define

$$\boldsymbol{u}_K^M = \boldsymbol{u}^M|_{\Theta_K^{\square}} \in \boldsymbol{H}^1(\Theta_K^{\square}) \,. \tag{82}$$

We denote $\tilde{\boldsymbol{u}}_K^M$ as the function that is zero outside of $\bar{\Theta}_K^{\square}$ and that is equal to the solution to the following local variational boundary-value problem of elastostatics,

$$\boxed{\begin{aligned} &\text{Find } \tilde{\boldsymbol{u}}_K^M \in \{\boldsymbol{u}_K^M\} + V(\Theta_K^{\square}) \text{ such that} \\ &\mathscr{B}_K(\tilde{\boldsymbol{u}}_K^M, \boldsymbol{v}_K) = \mathscr{F}_K(\boldsymbol{v}_K) \quad \forall\, \boldsymbol{v}_K \in V(\Theta_K^{\square}) \,, \end{aligned}} \tag{83}$$

where $\mathscr{B}_K : \boldsymbol{H}^1(\Theta_K^{\square}) \times \boldsymbol{H}^1(\Theta_K^{\square}) \mapsto \mathbb{R}$ is the bilinear form characterizing the local virtual work and $\mathscr{F}_K(\cdot)$ is a local linear functional characterizing the work done by the external forces:

$$\mathscr{B}_K(\tilde{\boldsymbol{u}}_K^M, \boldsymbol{v}_K) = \int_{\Theta_K^{\square}} \nabla\boldsymbol{v}_K : \boldsymbol{E}\nabla\tilde{\boldsymbol{u}}_K^M \, \mathrm{d}\boldsymbol{x} \qquad \mathscr{F}_K(\boldsymbol{v}_K) = \int_{\Theta_K^{\square}} \boldsymbol{f}\cdot\boldsymbol{v}_K \, \mathrm{d}\boldsymbol{x} + \int_{\Gamma_{\mathbf{Kt}}} \boldsymbol{t}\cdot\boldsymbol{v}_K \, \mathrm{d}s \,. \tag{84}$$

The displacements on $\Gamma_{\mathbf{Ku}}$ are prescribed as follows:

$$\tilde{\boldsymbol{u}}_K^M|_{\Gamma_{\mathbf{Ku}}} = \boldsymbol{u}_K^M|_{\Gamma_{\mathbf{Ku}}} \,. \tag{85}$$

On $\Gamma_{\mathbf{Kt}}$ the given external tractions, $\boldsymbol{t}$, are prescribed. The global solution is constructed in the following manner:

$$\tilde{\boldsymbol{u}}^M = \boldsymbol{u}^M + \mathscr{E}_1(\tilde{\boldsymbol{u}}_1^M - \boldsymbol{u}_1^M) + \mathscr{E}_2(\tilde{\boldsymbol{u}}_2^M - \boldsymbol{u}_2^M) + \cdots + \mathscr{E}_N(\tilde{\boldsymbol{u}}_N^M - \boldsymbol{u}_N^M) \,, \tag{86}$$

where it is natural to think of the above parenthetical terms as local perturbations to the homogenized solution $\boldsymbol{u}^M$. The question now becomes: if we were to solve the local problems and assemble the local solutions together (according to (86)), will the overall solution be improved? Consider the fact that the local problems are solved with inexact internal boundary conditions, which may be grossly in error. Fortunately, as we now shall see, this local construction and solution process will guarantee a superior solution in the energy norm.

THEOREM 5.5.1. Let $\boldsymbol{u}$ *be the exact solution to (7). Then with the previous definitions*

$$\|\tilde{\boldsymbol{u}}^M - \boldsymbol{u}\|_{E(\Omega)} \leq \|\boldsymbol{u}^M - \boldsymbol{u}\|_{E(\Omega)} \,. \tag{87}$$

PROOF. Let $\boldsymbol{u}^*$ be an arbitrary element, such that $\boldsymbol{u}^* \in \{\hat{\boldsymbol{u}}\} + V(\Omega)$. Then

$$\begin{aligned}\|u^* - u\|^2_{E(\Omega)} &= \mathcal{B}(u - u^*, u - u^*)\\ &= \mathcal{B}(u, u) + \mathcal{B}(u^*, u^*) - 2\mathcal{B}(u, u^*)\\ &= \mathcal{B}(u^*, u^*) - \mathcal{B}(u, u) - 2\mathcal{B}(u, u^*) + 2\mathcal{B}(u, u)\\ &= \mathcal{B}(u^*, u^*) - \mathcal{B}(u, u) - 2\mathcal{B}(u, u^* - u)\\ &= \mathcal{B}(u^*, u^*) - \mathcal{B}(u, u) - 2\mathcal{F}(u^* - u)\\ &= \mathcal{B}(u^*, u^*) - 2\mathcal{F}(u^*) - (\mathcal{B}(u, u) - 2\mathcal{F}(u))\\ &= 2\mathcal{T}(u^*) - 2\mathcal{T}(u)\,. \end{aligned} \tag{88}$$

Since each $\tilde{u}^M_K$ is solution to the local boundary value problem governed by (83), then each $\tilde{u}^M_K$ minimizes the local potential,

$$\mathcal{T}_K(w) = \frac{1}{2}\mathcal{B}_K(w, w) - \mathcal{F}_K(w) \quad \forall\, w \in \{u^M_K\} + V(\Theta^{\square}_K) \quad 1 \leq K \leq N(\mathcal{Q})\,. \tag{89}$$

Clearly, from the construction of the global function in (86)

$$\mathcal{J}(u^M) = \sum_K \mathcal{T}_K(u^M_K) \geq \sum_K \mathcal{T}_K(\tilde{u}^M_K) = \mathcal{T}(\tilde{u}^M)\,. \tag{90}$$

Therefore

$$\mathcal{T}(\tilde{u}^M) - \mathcal{T}(u) \leq \mathcal{T}(u^M) - \mathcal{T}(u)\,. \tag{91}$$

From (88) the desired result follows,

$$\|\tilde{u}^M - u\|_{E(\Omega)} \leq \|u^M - u\|_{E(\Omega)}\,. \quad \square \tag{92}$$

5.5.1. Observations

We make three important observations.

(1) For three-dimensional problems, the computational cell size is on the order of the inhomogeneity size, the cost of the HDPM procedure, in terms of operation counts, is N times cheaper than solving a problem with a direct numerical discretization technique, where N is the number of subdomains. Since the subdomain problems are completely decoupled, parallel processing techniques can be employed. As a consequence, one may attempt to also reduce the time to solution further by a factor of P, where P is the number of (equal speed) processors available.

(2) With the HDPM construction of the local problems, we can bound the difference in the homogenized solution and its local perturbation, the '*sensitivity*' beforehand. In other words, we may determine *locally* where the local solution process will produce a significant change in the solution. With the construction of the local problems in Theorem 5.5 we have, directly from Theorem 3.1,

$$\|\tilde{u}^M - u^M\|_{E(\Theta^{\square}_K)} \leq \|\|\mathcal{J}_M \nabla u^M\|\|_{E(\Theta^{\square}_K)} \quad \forall\, \Theta^{\square}_K \in \mathcal{Q},\ K = 1, 2, \ldots, N(\mathcal{Q})\,. \tag{93}$$

Note that the quantity on the right-hand side of (93) has been bounded beforehand, and is identical to the local error indicator, and therefore incurs no extra work, if the same partitions are used.

(3) Central to the success of the method is the choice of $\boldsymbol{E}^M$ to minimize the final solution error, $\|u - \tilde{u}^M\|_{E(\Omega)}$. The final error can be characterized in a straightforward manner. For any admissible virtual displacement v, we have

$$\begin{aligned}\int_\Omega \nabla(u - \tilde{u}^M) : \boldsymbol{E}\nabla v \, dx &= \int_\Omega f \cdot v \, dx + \int_{\Gamma_t} t \cdot v \, ds - \int_\Omega \nabla \tilde{u}^M : \boldsymbol{E}\nabla v \, dx\\ &= \sum_{\Theta^{\square}_K} \left\{ \int_{\Theta^{\square}_K} f \cdot v \, dx + \int_{\Gamma_{Kt}} t \cdot v \, ds - \int_{\Theta^{\square}_K} \nabla \tilde{u}^M : \boldsymbol{E}\nabla v \, dx \right\}. \end{aligned} \tag{94}$$

Noting that $\nabla\cdot(\boldsymbol{E}\nabla\boldsymbol{u}\cdot\boldsymbol{v})-\nabla\cdot(\boldsymbol{E}\nabla\boldsymbol{u})\cdot\boldsymbol{v}=\boldsymbol{E}\nabla\boldsymbol{u}:\nabla\boldsymbol{v}$, and using the divergence theorem, we have

$$\int_\Omega \nabla(\boldsymbol{u}-\tilde{\boldsymbol{u}}^M):\boldsymbol{E}\nabla\boldsymbol{v}\,\mathrm{d}\boldsymbol{x}=\sum_{\Theta_K^\square}\left\{\int_{\Theta_K^\square}(\boldsymbol{f}+\nabla\cdot(\boldsymbol{E}\nabla\tilde{\boldsymbol{u}}^M))\cdot\boldsymbol{v}\,\mathrm{d}\boldsymbol{x}\right.$$
$$\left.+\int_{\Gamma_{\mathbf{Kt}}}(\boldsymbol{t}-\boldsymbol{E}\nabla\tilde{\boldsymbol{u}}^M\cdot\boldsymbol{n}_K)\cdot\boldsymbol{v}\,\mathrm{d}\boldsymbol{s}-\int_{\Gamma_{\mathbf{Ku}}}\boldsymbol{E}\nabla\tilde{\boldsymbol{u}}\cdot\boldsymbol{n}_K\cdot\boldsymbol{v}\,\mathrm{d}\boldsymbol{s}\right\}$$
$$=0+0-\sum_{\Theta_K^\square}\left\{\int_{\Gamma_{\mathbf{Ku}}\setminus\Gamma_{\mathbf{u}}}\boldsymbol{E}\nabla\tilde{\boldsymbol{u}}^M\cdot\boldsymbol{n}_K\cdot\boldsymbol{v}\,\mathrm{d}\boldsymbol{s}\right\}. \tag{95}$$

Therefore

$$\|\boldsymbol{u}-\tilde{\boldsymbol{u}}^M\|^2_{E(\Omega)}=\sum_{\Theta_K^\square}\int_{\Gamma_{\mathbf{Ku}}\setminus\Gamma_{\mathbf{u}}}\boldsymbol{E}\nabla\tilde{\boldsymbol{u}}^M\cdot\boldsymbol{n}_K\cdot(\boldsymbol{u}^M-\boldsymbol{u})\,\mathrm{d}\boldsymbol{s}\,. \tag{96}$$

The right-hand side can be interpreted as the work done by the jumps in traction moving through the difference in the actual and homogenized displacement on interior subdomain boundaries. Critical to the success of the method is, therefore, the choice of $\boldsymbol{E}^M$ to minimize the work done by the traction jumps on the subdomain boundaries. The choice for $\boldsymbol{E}^M$ is certainly problem-dependent.

5.5.2. Example 1: Applying HDPM directly to the (zero-scale) homogenized solution

In this example, we illustrate the dependence of the HDPM solution on the choice of $\boldsymbol{E}^M$. To this end, we return to one-dimensional example considered before, and first consider $M=0$, $\boldsymbol{E}^0$. The fine-scale and homogenized problems are

$$\frac{\mathrm{d}}{\mathrm{d}x}\left(E(x)\frac{\mathrm{d}u(x)}{\mathrm{d}x}\right)=-1\,,\qquad u(0)=0\,,\qquad u(1)=0 \tag{97}$$

and

$$\frac{\mathrm{d}}{\mathrm{d}x}\left(E^M(x)\frac{\mathrm{d}u^M(x)}{\mathrm{d}x}\right)=-1\,,\qquad u^M(0)=0\,,\qquad u^M(1)=0\,. \tag{98}$$

For each subdomain $K=1,\ldots,N(\mathcal{Q})$, the local HDPM problem is

$$\frac{\mathrm{d}}{\mathrm{d}x}\left(E(x)\frac{\mathrm{d}\tilde{u}_K^M(x)}{\mathrm{d}x}\right)=-1\,,\qquad x\in(X_K,X_{K+1})\qquad \tilde{u}_K^M(X_K)=u^M(X_K)\,,$$

$$\tilde{u}_K^M(X_{K+1})=u^M(X_{K+1})\,, \tag{99}$$

where X_K, X_{K+1} are the endpoints of each subdomain (Figs. 7 and 8).

In our example, the unit interval is divided into 10 000 equal intervals, and for each interval the property is chosen at random either $E=1$ or $E=\tau$, where τ is the mismatch ratio. Equal amounts of hard and soft material are used. A coarser partition is overlaid representing the subdomain partition. All of the following calculations are done *analytically*. For convenience, and to illustrate the sensitivity of the results to the choice of $\boldsymbol{E}^M$, we choose the classical upper and lower bounds in (32).

From Tables 5 and 6 it is clear that the *harmonic* average ($\boldsymbol{E}^M=\langle\boldsymbol{E}^{-1}\rangle^{-1}$) produces far superior final solutions. This is due to the fact that the internal boundary conditions are of displacement type and that the harmonic average produces the superior overall displacement compared to that of the arithmetic average. In this one-dimensional case, the flux jumps play a minor role, and therefore the error is essentially governed by the quality of the displacement data. Of course, in general, we seek an $\boldsymbol{E}^M$ that produces the exact displacement on the internal subdomain boundaries. Initially, the solution produced by the harmonic average is in gross error, but after HDPM it has a far superior solution, with respect to the energy norm compared to that of the arithmetic average. Increasing the number of subdomains

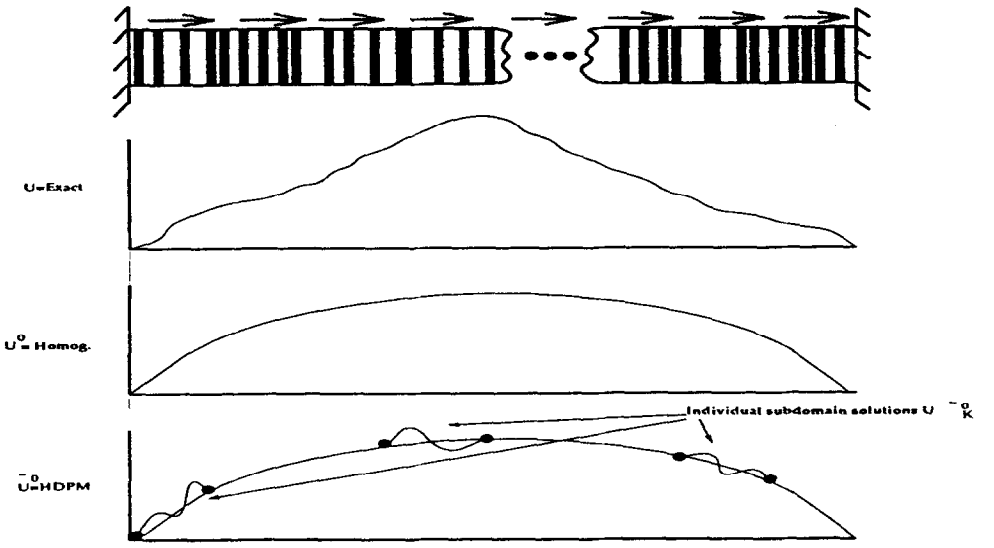

Fig. 7. The heterogenous bar, with depictions of the exact solution, the homogenized solution, and local perturbations to the homogenized solution.

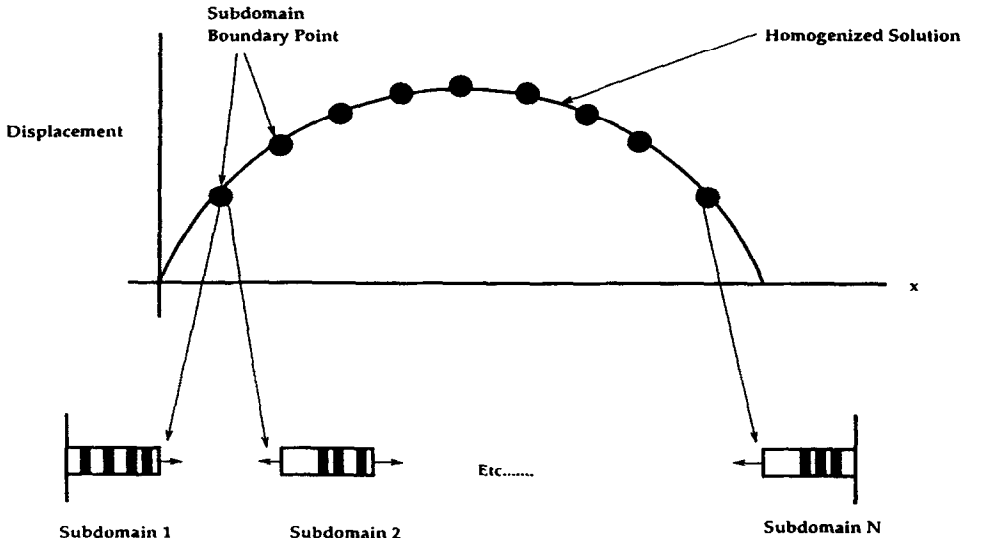

Fig. 8. The heterogeneous bar, and construction of the local problems.

Table 5
The homogenized solution error and HDPM error for $\boldsymbol{E}^M = \langle \boldsymbol{E} \rangle$ for 100 subdomains and 10 subdomains, versus mismatch ratio

τ	$\|\boldsymbol{u}\|_{E(\Omega)}$	$\|\boldsymbol{u}-\boldsymbol{u}^0\|_{E(\Omega)}/\|\boldsymbol{u}\|_{E(\Omega)}$	$\|\boldsymbol{u}-\tilde{\boldsymbol{u}}^M\|_{E(\Omega)}/\|\boldsymbol{u}\|_{E(\Omega)}$ $N=100,\ 10$
10	0.185284	0.804457	0.649229 0.644998
50	0.173124	0.956960	0.916105 0.911536
100	0.171544	0.978203	0.957011 0.952321

Table 6
The homogenized solution error and HDPM error for $E^M = \langle E^{-1} \rangle^{-1}$ for 100 subdomains and 10 subdomains, versus mismatch ratio

τ	$\|u\|_{E(\Omega)}$	$\|u - u^0\|_{E(\Omega)} / \|u\|_{E(\Omega)}$	$\|u - \tilde{u}^0\|_{E(\Omega)} / \|u\|_{E(\Omega)}$ $N = 100$, 10
10	0.185284	1.347399	0.100066 0.032339
50	0.173124	3.276713	0.125849 0.040390
100	0.171544	4.680409	0.129001 0.041567

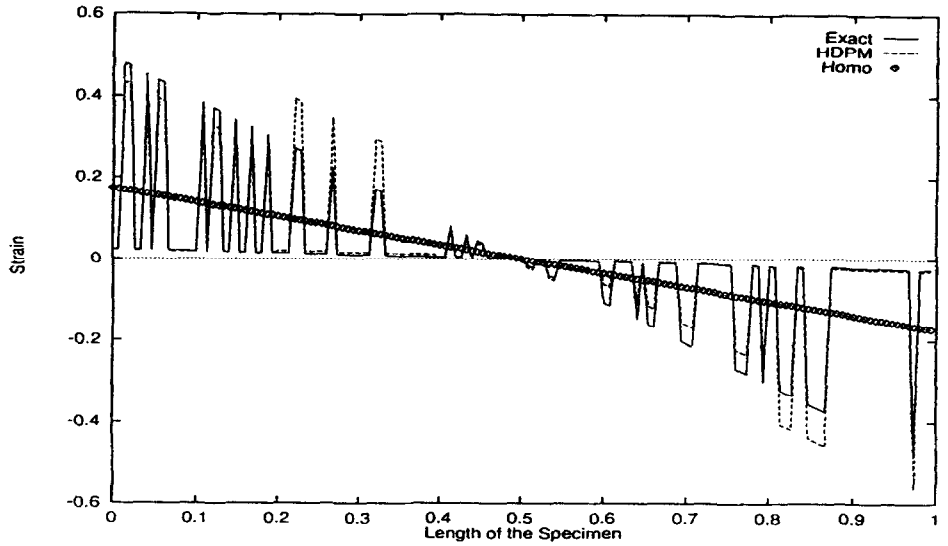

Fig. 9. A mismatch of 20 : 1 with 150 intervals, each with randomly assigned material properties. HPDM with 5 subdomains, using the harmonic average solution to construct local boundary conditions.

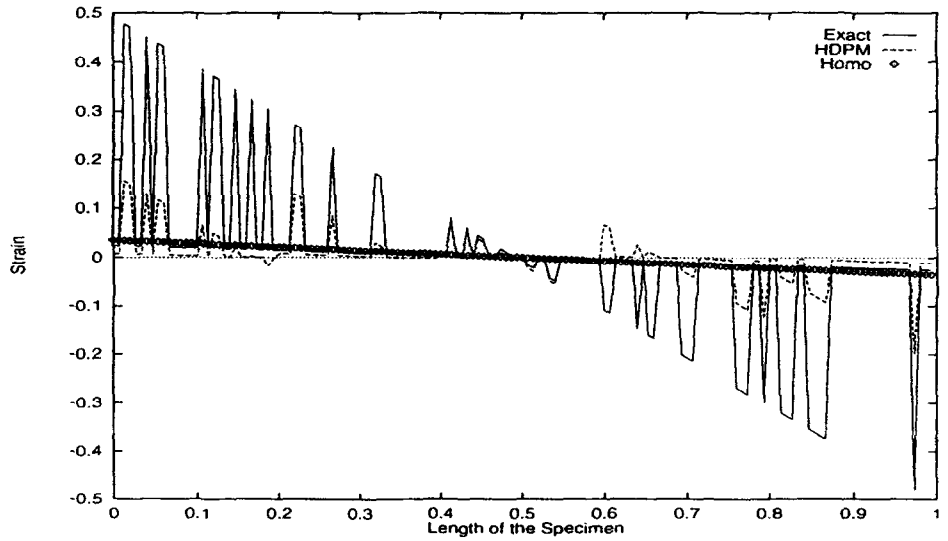

Fig. 10. A mismatch of 20 : 1 with 150 intervals, each with randomly assigned material properties. HPDM with 5 subdomains, using the arithmetic average solution to construct local boundary conditions.

produces a solution which is increasingly worse, since more inexact information is introduced on more subdomain boundaries.

Strain fields for cases with less material variations, which are easier to visualize on the printed page, are included in Figs. 9 and 10, and it can be seen that for the harmonic averaging case the HDPM solution seems to capture local fluctuations in the solution quite well.

In the one-dimensional example, among the two effective material choices of $\boldsymbol{E}^M$ tested, the selection is straightforward, the harmonic average delivers a superior final solution. As we have noted, in higher dimensions this choice is unclear.

5.5.3. *Example 2: Applying HDPM to the ALR generated solutions*

Returning to the heterogeneous bar, we now apply HDPM to the ALR solutions. The main points to be observed in this example are that further error reduction, beyond applying HDPM directly to the zero-scale solution, $\boldsymbol{u}^0$, can be made by using hierarchical structures generated by ALR. We present two levels of *uniform* refinement of the material description. Level 0 corresponds to a solution generated by a uniform elasticity throughout the body; level 1 corresponds to a solution generated by using an elasticity corresponding to the average in each subdomain; level 2 corresponds to solution generated by using material properties obtained by bisecting each subdomain and averaging the material property over each subdomain half (Fig. 5). All calculations were done analytically. For convenience, and to illustrate the dependence of the final solution on the choice of the local reaveraging technique, we locally reaverage according to the classical bounds, $\langle \boldsymbol{E} \rangle$ and $\langle \boldsymbol{E}^{-1} \rangle^{-1}$.

As before, even when ALR and HDPM are combined, Tables 7 and 8 illustrate that *the choice of the*

Table 7
The level 0, 1 and 2 solution errors for $\boldsymbol{E}^0 = \langle \boldsymbol{E} \rangle$, 10 000 material variations, 10 subdomains with increasing mismatch ratio

τ	$\|\boldsymbol{u} - \tilde{\boldsymbol{u}}^0\|_{E(\Omega)} / \|\boldsymbol{u}\|_{E(\Omega)}$	$\|\boldsymbol{u} - \tilde{\boldsymbol{u}}^1\|_{E(\Omega)} / \|\boldsymbol{u}\|_{E(\Omega)}$	$\|\boldsymbol{u} - \tilde{\boldsymbol{u}}^2\|_{E(\Omega)} / \|\boldsymbol{u}\|_{E(\Omega)}$
10	0.644998	0.643914	0.643644
50	0.911536	0.911260	0.911179
100	0.952321	0.952175	0.952134

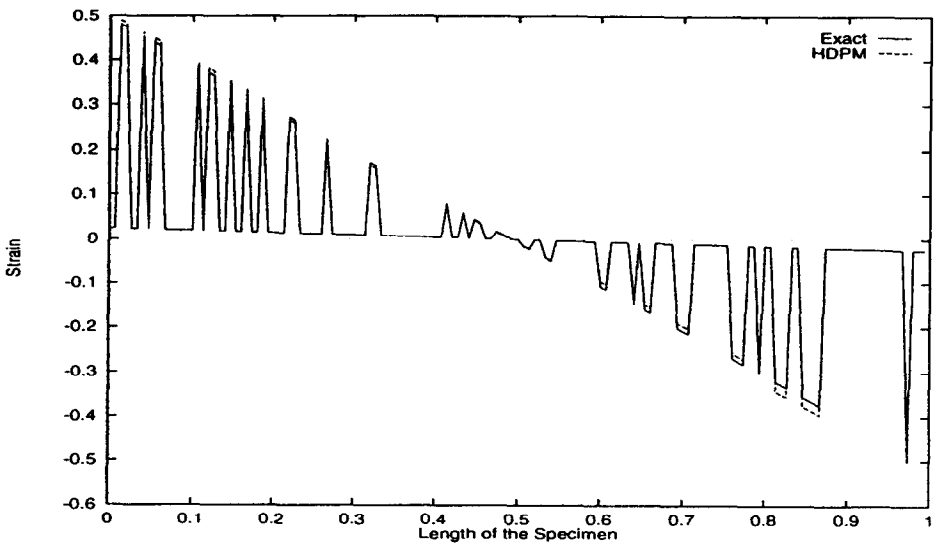

Fig. 11. Level 1 scale used for HDPM. A mismatch of 20 : 1 with 150 intervals, each with randomly assigned material properties. HDPM with 5 subdomains, using the harmonic average solution to construct local boundary conditions.

Table 8
The level 0, 1 and 2 solution errors for $\boldsymbol{E}^0 = \langle \boldsymbol{E}^{-1} \rangle^{-1}$, 10 000 material variations, 10 subdomains with increasing mismatch ratio

τ	$\|\boldsymbol{u} - \tilde{\boldsymbol{u}}^0\|_{E(\Omega)} / \|\boldsymbol{u}\|_{E(\Omega)}$	$\|\boldsymbol{u} - \tilde{\boldsymbol{u}}^1\|_{E(\Omega)} / \|\boldsymbol{u}\|_{E(\Omega)}$	$\|\boldsymbol{u} - \tilde{\boldsymbol{u}}^2\|_{E(\Omega)} / \|\boldsymbol{u}\|_{E(\Omega)}$
10	0.032339	0.004203	0.002629
50	0.040390	0.005244	0.003283
100	0.041567	0.005392	0.003377

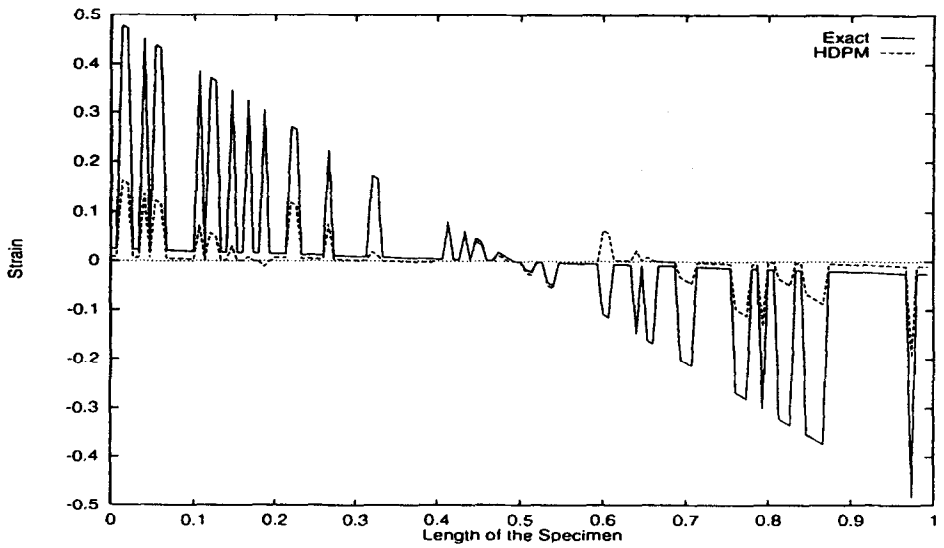

Fig. 12. Level 1 scale used for HDPM. A mismatch of 20 : 1 with 150 intervals, each with randomly assigned material properties. HDPM with 5 subdomains, using the arithmetic average solution to construct local boundary conditions.

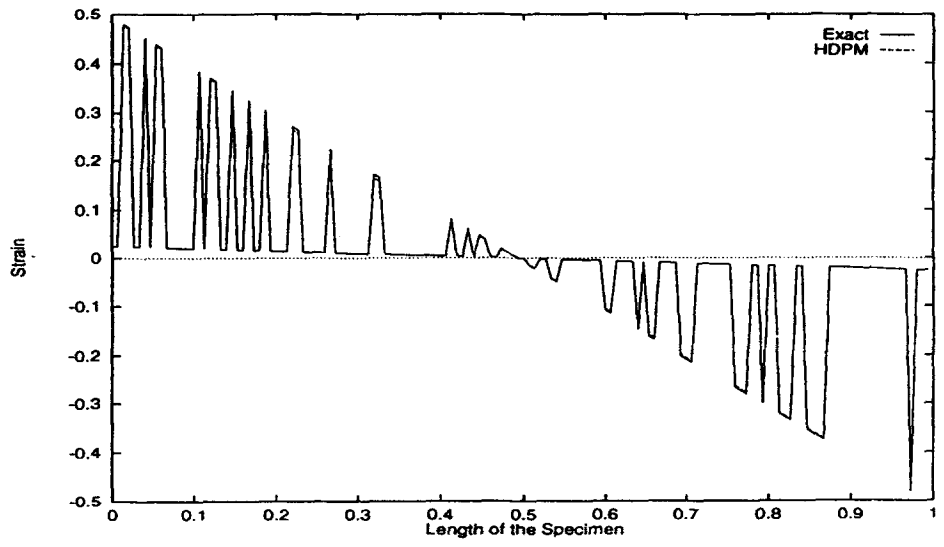

Fig. 13. Level 2 scale used for HDPM. A mismatch of 20 : 1 with 150 intervals, each with randomly assigned material properties. HDPM with 5 subdomains, using the harmonic average solution to construct local boundary conditions.

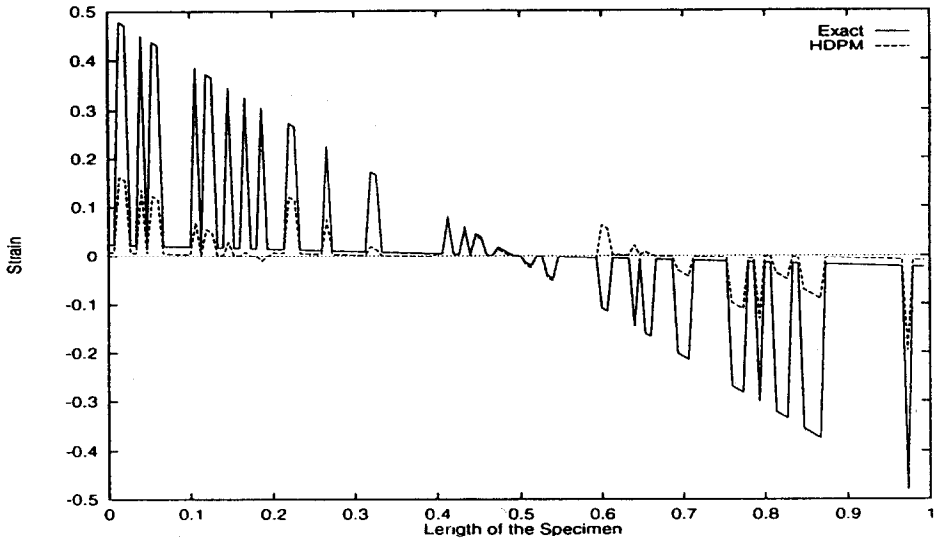

Fig. 14. Level 2 scale used for HDPM. A mismatch of 20 : 1 with 150 intervals, each with randomly assigned material properties. HDPM with 5 subdomains, using the arithmetic average solution to construct local boundary conditions.

(local) homogenized properties is critical to the quality of the final solution. It is possible, as illustrated in Table 8 to achieve error that is on the order of a fraction of a percent, for this one-dimensional problem. Figs. 11–14 make a clear point that the methods produce extremely accurate resolution of the strain field locally. As can be seen, for this example, in the harmonic averaging case, one may obtain more than one order of magnitude reduction of the error after only two levels of refinement.

OBSERVATION. One can interpret the ALR solutions as providing better local boundary conditions for subdomains in HDPM, and in this light, the method as a whole can be thought of as a non-overlapping domain decomposition method [9].

6. Summary

In this paper a methodology that consists of the following three main ideas has been introduced:

(1) A global explicit estimate of the solution error introduced in using a homogenized (coarse) elasticity tensor and using the actual fine-scale elasticity tensor is derived. This estimate only requires the calculation of the coarse-scale solution. Numerical experiments suggest that the estimate gives reasonable estimation of the local error as well.

(2) A procedure for generating a hierarchical family of material descriptions and corresponding solutions is developed. The solutions corresponding to the members of the hierarchy are shown to converge to the solution of the fine-scale problem in an energy norm. In this method, the fine-scale model of a structural component, which embodies the exact material description, represents the highest level of sophistication in a family of continuum models.

(3) A post-processing procedure which endows the coarse-scale solutions with fine-scale information is developed. The process requires the solution of local, decoupled subproblems posed on subdomains inside the body. This process is trivially parallelizable, due to the decoupled nature of the method. It is proven that the solutions generated by this 'post-processing' procedure will always yield superior solutions to the original coarse-scale solution. Error reductions of orders of magnitude over the classical homogenized solution realized in simple one-dimensional examples and may also be obtainable in higher dimensions.

Acknowledgment

The authors would like to thank Drs Leszek Demkowicz and Peter Shi for insightful discussions related to the presented subject matter. The authors gratefully acknowledge the support of this work by National Science Foundation under grant ECS-9422707 and the Office of Naval Research under grant 95-J-0401.

References

[1] J. Fish and V. Belsky, Multigrid method for periodic heterogeneous media Part I: Convergence studies for one dimensional case, Comput. Methods Appl. Mech. Engrg. 126 (1995).
[2] J. Fish and V. Belsky, Multigrid method for periodic heterogenous media Part II: Multiscale modeling and quality control in multidimensional case, Comput. Methods Appl. Mech. Engrg. 126 (1995).
[3] S. Ghosh and S.N. Mukhopadhyay, A material based finite element analysis of heterogeneous media involving Dirichlet tessalations, Comput. Methods Appl. Mech. Engrg. 104 (1993) 211–247.
[4] S. Ghosh and S.N. Moorthy, Elastic-plastic analysis of heterogeneous microstructures using the Voronoi-cell finite element method, Comput. Methods Appl. Mech. Engrg., to appear.
[5] S. Hasanov and C. Huet, Order relationships for boundary conditions effect in heterogeneous bodies smaller than the representative volume, J. Mech. Phys. Solids 42 (1994) 1995–2011.
[6] R. Hill, The elastic behaviour of a crystalline aggregate, Proc. Phys. Soc. (Lond.) A65 (1952) 349–354.
[7] C. Huet, Application of variational concepts to size effects in elastic heterogeneous bodies, J. Mech. Phys. Solids 38 (1990) 813–841.
[8] V.V. Jikov, S.M. Kozlov and O.A. Olenik, Homogenization of Differential Operators and Integral Functionals (Springer-Verlag, 1994).
[9] P. Le Tallec, Domain decomposition methods in computational mechanics, Comput. Mech. Adv. 1(2) (1994).
[10] J.T. Oden and G.F. Carey, Finite Elements: Mathematical Aspects, Vol. IV (Prentice-Hall, Englewood Cliffs, NJ, 1983).